



# Phase Behaviour of Colloidal Rods Mixed with Depletants

# 8

So far, we have considered the phase behaviour of colloidal spheres mixed with depletants. In Chap. 3, we considered the simplest type of depletant, the penetrable hard sphere (PHS). We then extended this treatment to ideal and excluded volume polymers in Chap. 4; and in Chap. 6, we considered small colloidal spheres (including micelles). Colloidal rods as depletants were addressed in Chap. 7; however, Chap. 7 only considered dilute dispersions of rods, in which the rods assume all configurations and are hence isotropic. In this chapter, we consider the phase behaviour of mixtures of colloidal rods and polymeric depletants, and we also account for higher rod concentrations and the corresponding phase states.

## 8.1 Experimental Observations with Rod-Like Particle Dispersions

Colloidal rods can be subdivided into synthetic inorganic rods, rod-like clay particles and biological rods (see also [1]). Examples are given in Fig. 8.1. Suspensions of rod-like particles exhibit interesting phase transitions and can assume various phase states. For a description of the various liquid crystalline phases, we refer the reader to the standard textbook on liquid crystals by de Gennes and Prost [2]. Lyotropic liquid crystalline phases were recognised a long time ago in suspensions of rod-like inorganic vanadium pentoxide ( $V_2O_5$ ) colloids by Zocher [3], and later in solutions of biological particles comprising the tobacco mosaic virus (TMV) by Bawden et al. [4].

Upon concentrating a dilute rod suspension, a transition from an isotropic phase to an orientationally ordered phase occurs for rods with a length–diameter ratio  $L/D > 3.5$ . This is the so-called nematic liquid crystal phase, for which examples are given in Figs. 8.2 and 8.3. The first step of the isotropic–nematic phase transition

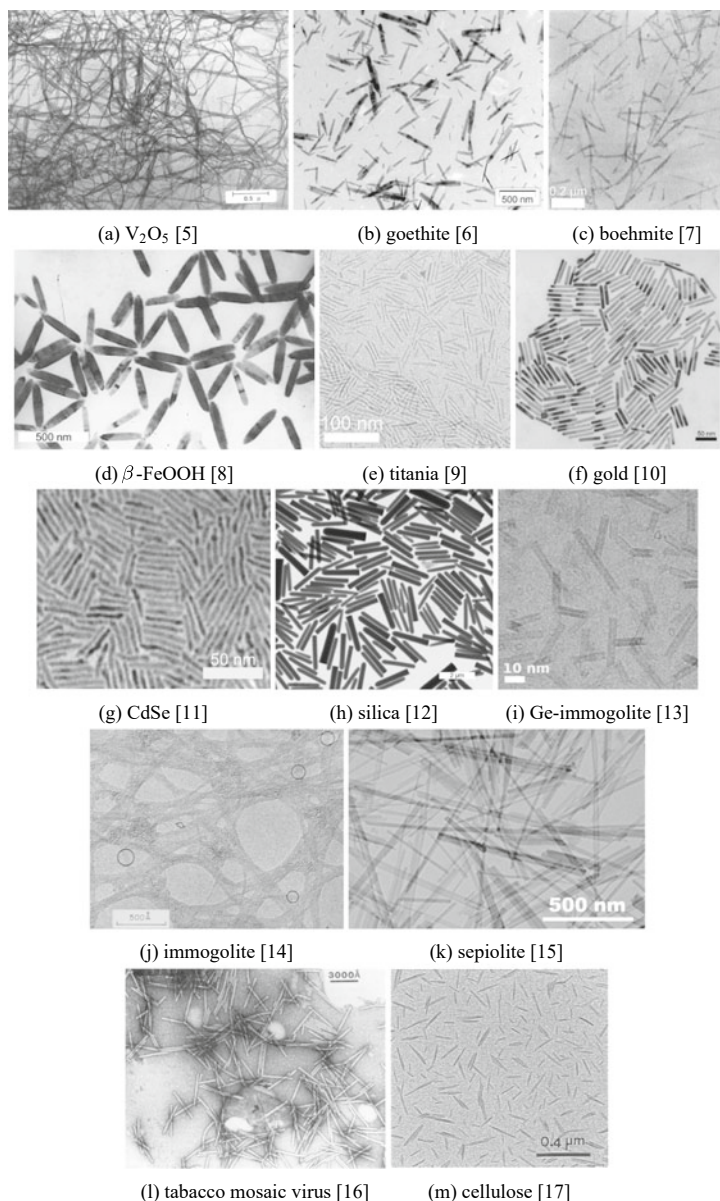


**Fig. 8.1** Transmission electron microscopy (TEM) micrographs of **a–i** synthetic inorganic, **j, k** clay and **l, m** biological rod-like colloids. Reprinted with permission from **a** Ref. [5], copyright 1991 American Chemical Society (ACS); **b** Ref. [6], copyright 2006 ACS; **c** Ref. [7], copyright 1994 ACS; **d** Ref. [8], copyright 1996 ACS; **e** Ref. [9], copyright 2020 Wiley; **f** Ref. [10], copyright 2009 Elsevier; **g** Ref. [11], copyright 2002 ACS; **h** Ref. [12], copyright 2011 ACS; **i** Ref. [13], copyright 2013 the Royal Society of Chemistry (RSC); **j** Ref. [14], copyright 1970 Cambridge University Press; **k** Z. Zhang, Soochow University, China; **l** Ref. [16], copyright 1985 EDP Sciences; **m** Ref. [17], copyright 1996 ACS

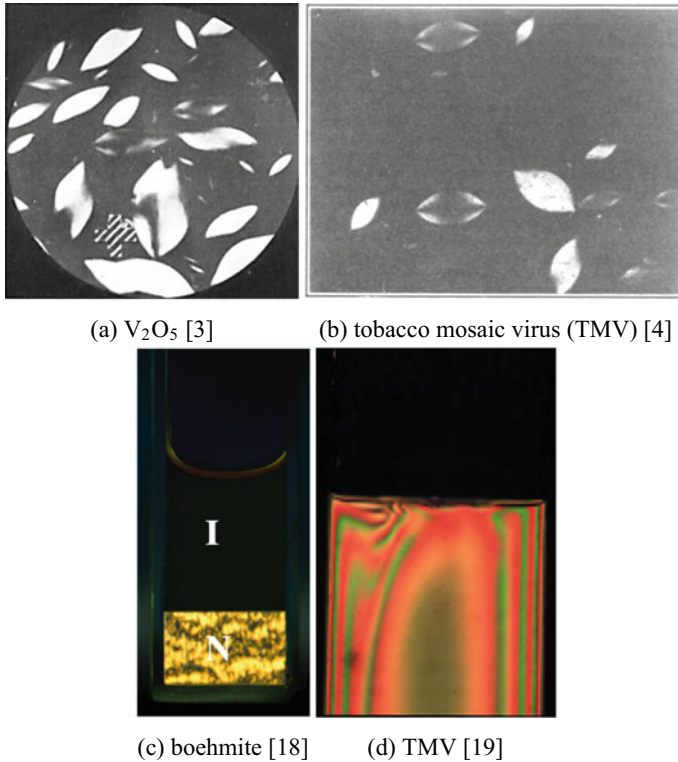


**Fig. 8.2** Examples of **a, b** nematic tactoids and **c, d** macroscopic isotropic–nematic phase coexistence observed between crossed polarisers. Reprinted with permission from: **a** Ref. [3], copyright 1925 Wiley; **b** Ref. [4], copyright 1936 Nature; **c** P. A. Buining, Utrecht University; **d** Ref. [19], copyright 2006 Wiley

is the formation of spindle-like droplets (so-called tactoids) of the nematic phase that float in the isotropic phase (Fig. 8.2a, b). Over time, these droplets coalesce to give rise to a macroscopic nematic bottom phase and an isotropic top phase. The rods have a different refractive index in parallel and perpendicular directions. As a result, the nematic phase displays typical interference colours under crossed polarisers due to a difference in retardation of light in different directions (Fig. 8.2c, d).

Oster [24] found an additional liquid crystal phase in suspensions of TMV in which the particles are ordered in periodic layers. On average, the axes of the rods are perpendicular to the layers (Fig. 8.3) and within the layers the rods behave like a two-dimensional fluid. This phase is known as the smectic A phase (SmA) [2]. For a long time, it was argued that attractive interactions between the rods were necessary for the occurrence of this phase. Frenkel, Stroobants and Lekkerkerker [25], however, showed by using Monte Carlo simulations that smectic ordering occurs in a fluid of hard rod-like particles, i.e., a smectic phase may appear solely driven by entropy.

Figure 8.3b–d gives examples of confocal microscopy images of silica rod suspensions with  $L/D \approx 6$ . Upon increasing the silica rod concentration, Kuijk et al. [22]

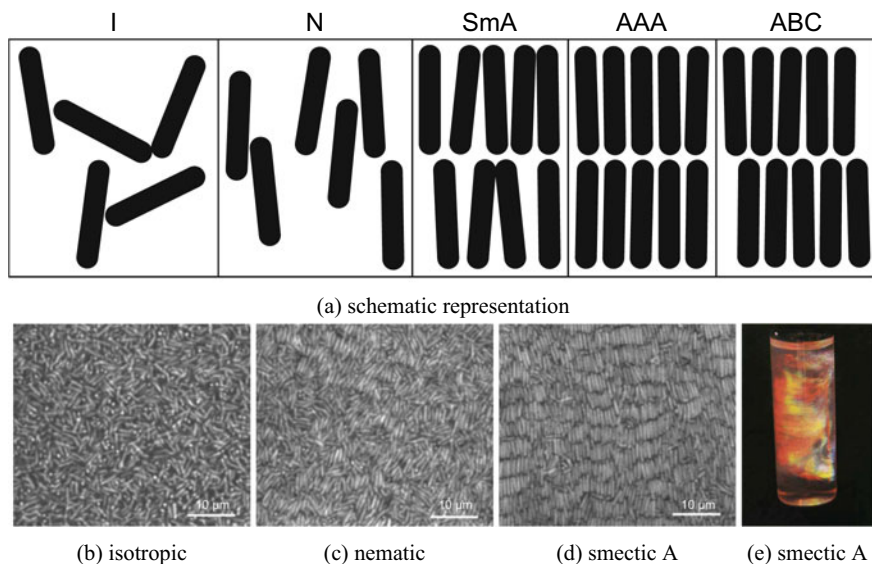


**Fig. 8.3** **a** Sketches [20,21] and **b–d** experimental observations [22] of the structure of different phases of silica rods. **e** Iridescence observed in a smectic liquid crystal of TMV [23]. Reprinted with permission from **a** Peters et al. [20] under the terms of CC-BY-4.0; **b–d** Ref. [22], copyright 2012 RSC and **e** Ref. [23], copyright 1985 Wiley

found isotropic (b), nematic (c) and smectic ordering (d) also. The layered structure of the SmA with layer distances of the order of the wavelength of light gives rise to impressive iridescence (see Fig. 8.3e). Computer simulations have revealed that hard rods can also give rise to crystal phases AAA and ABC at high rod densities (see Fig. 8.3a) [26,27].

The effect of nonadsorbing polymer on the isotropic–nematic phase transition has been studied since the 1940s with a focus on the practical possibilities of isolation and separation of viruses [28,29] (see Sect. 1.3.2.4). It was observed that the addition of relatively small amounts of polymer to virus suspensions led to the ‘precipitation’ of the virus particles (i.e., the formation of a concentrated phase of the virus particles). Only much later in the 1990s were experiments initiated on model suspensions of rod-like colloids mixed with polymers to study the treatment given in the previous chapters to rod-like colloids mixed with depletant, and the results compared to theory and computer simulations.

To connect the experimental observations discussed here to theoretical predictions, we first discuss the Onsager theory (Sect. 8.2) to quantify the I–N phase transition of long hard rods and its extension to describe charged rods. Subsequently, scaled particle theory of rods is discussed to approximate finite size effects of rods in Sect. 8.3. In Sect. 8.4, theory for the phase behaviour of mixtures of hard rods and nonadsorbing polymers is presented, and experimental examples are provided in

Sect. 8.5. Finally, higher order phase states are included in the theoretical description in Sect. 8.6. All sections are supplemented by comparison with experiment and/or computer simulation results.

## 8.2 Onsager Theory of the Isotropic–Nematic Transition

### 8.2.1 Long Hard Rods

As we saw in the previous chapters, colloidal phase transitions of hard particles are governed by entropy. This was first revealed by Onsager, who showed that the isotropic–nematic (I–N) phase transition in assemblies of hard rods is driven solely by entropy. He realised that an attractive force is not necessary for the I–N transition by showing that an assembly of repelling rods exhibits a transition from an isotropic to a nematic state due to a gain of packing entropy that compensates the loss of orientational entropy. Onsager also demonstrated that the I–N transition may be treated within a virial expansion of the free energy. In fact, this is a unique example of a phase transition that can be treated using a virial expansion. For very thin, rigid, hard particles the transition occurs at a very low volume fraction and the virial expansion may even be truncated after the second virial term, leading to an exact theory for infinitely thin particles. In the following, we give a brief exposition on Onsager’s theory. For more details, we refer the reader to [30,31].

The Helmholtz free energy  $F$  for a dispersion of  $N$  hard rods (which we, as in Sect. 7, model as spherocylinders with length  $L$  and diameter  $D$ ) in a volume  $V$  in the second virial approximation can be written as

$$\frac{F[f]}{NkT} = \text{constant} - 1 + \ln c + s[f] + c\rho[f]. \quad (8.1)$$

We have lumped in the constant quantities that do not affect the phase transition, i.e., have the same value in the coexisting phases. The quantity  $c$  is the dimensionless concentration

$$c = bn, \quad (8.2)$$

where  $b = (\pi/4)L^2D$  is the excluded volume and  $n = N/V$  is the number density of the rods. The orientational entropy is expressed through  $s[f]$ :

$$s_{\text{or}} = -k \int f(\mathbf{\Omega}) \ln[4\pi f(\mathbf{\Omega})] d\mathbf{\Omega} = -ks[f], \quad (8.3)$$

where  $f(\mathbf{\Omega})$  is the orientational distribution function, which gives the probability of finding a spherocylinder with an orientation characterised by the solid angle  $\mathbf{\Omega}$ . Finally,  $-kc\rho[f]$  is the packing entropy per particle, with

$$\rho[f] = \frac{4}{\pi} \int \int |\sin \gamma| f(\mathbf{\Omega}) f(\mathbf{\Omega}') d\mathbf{\Omega} d\mathbf{\Omega}', \quad (8.4)$$

where  $\gamma$  is the angle between the rods, which depends on their orientations  $\mathbf{\Omega}$  and  $\mathbf{\Omega}'$  (see Fig. 7.4).

As already remarked, the I–N transition originates from a competition between the orientational and packing entropy. For low concentrations the orientational entropy dominates and attains a maximum value for an isotropic distribution  $f = (4\pi)^{-1}$ ; whereas for high concentrations the packing entropy becomes more important, favouring a nematic orientation distribution. The orientational distribution is determined by the fact that the free energy must be a minimum. Upon minimising Eq. (8.1), the integral equation

$$\ln[4\pi f(\theta)] = \lambda - \frac{8c}{\pi} \int |\sin \gamma(\mathbf{\Omega}, \mathbf{\Omega}')| f(\theta') d\mathbf{\Omega}' \quad (8.5)$$

is obtained. Here, we have taken into account that  $f$  does not depend on the azimuthal angle but only on  $\theta$ , the polar angle between the rod vector and the nematic vector. Furthermore, the distribution function  $f(\theta)$  must satisfy inversion symmetry, implying the angles  $\theta$  and  $\pi - \theta$  are equivalent. Note that we assume the nematic phase is apolar. The Lagrange multiplier  $\lambda$  is determined by requiring that  $f(\theta)$  fulfils the normalisation condition

$$\int f(\mathbf{\Omega}) d\mathbf{\Omega} = 1. \quad (8.6)$$

It is easily seen that the isotropic distribution function

$$f = \frac{1}{4\pi} \quad (8.7)$$

satisfies Eq. (8.5) for all concentrations (although it is only for low concentrations that this corresponds to a minimum of the free energy). For the isotropic phase,  $\mathfrak{s}$  and  $\rho$  attain the values

$$\mathfrak{s}_I = 0, \quad \rho_I = 1, \quad (8.8)$$

and hence

$$\frac{F_I}{NkT} = \text{constant} - 1 + \ln c + c. \quad (8.9)$$

---

**Exercise 8.1.** Derive Eq. (8.8) from Eqs. (8.3) and (8.4) using Eq. (8.7).

---

An exact solution to the non-linear integral equation Eq. (8.5) for higher concentrations, where a nematic distribution minimises the free energy, has not yet been found but ways to solve it numerically have appeared [32,33]. For a didactic account of how to solve Eq. (8.5) numerically, see Ref. [34]. This allows the determination of  $\mathfrak{s}[f]$  and  $\rho[f]$  and, from thereon, the free energy in the nematic phase. To be

in mechanical and chemical equilibrium, both phases must have the same osmotic pressure and the same chemical potential (see Eqs. (A.13) and (A.14)),

$$P_I(c_I) = P_N(c_N), \quad (8.10a)$$

$$\mu_I(c_I) = \mu_N(c_N). \quad (8.10b)$$

These quantities can be obtained (see Appendix A) from the free energy using the standard thermodynamic relations:

$$P = - \left( \frac{\partial F}{\partial V} \right)_{N,T}, \quad (8.11a)$$

$$\mu = \left( \frac{\partial F}{\partial N} \right)_{V,T}. \quad (8.11b)$$

For the isotropic phase, we find from Eq. (8.9)

$$\frac{P_I b}{kT} = c_I + c_I^2, \quad (8.12a)$$

$$\frac{\mu_I}{kT} = \text{constant} + \ln c_I + 2c_I. \quad (8.12b)$$

---

**Exercise 8.2.** Show that Eqs. (8.12a) and (8.12b) follow from Eqs. (8.9) and (8.11a) and (8.11b).

---

In the nematic phase, Eq. (8.1) gives

$$\frac{P_N b}{kT} = c_N + c_N^2 \rho[f], \quad (8.13a)$$

$$\frac{\mu_N}{kT} = \text{constant} + \ln c_N + \mathfrak{s}[f] + 2c_N \rho[f]. \quad (8.13b)$$

where the distribution  $f$  must be obtained numerically for each concentration from Eq. (8.5). Solving the coexistence equations (8.10a) and (8.10b) with the above expressions for the osmotic pressure and chemical potential numerically yields the coexistence concentrations

$$c_I = 3.290, \quad c_N = 4.191. \quad (8.14)$$

The usual measure of the ordering in the nematic phase is given by the nematic order parameter  $S$ , which is defined as

$$S = \int \mathcal{P}_2(\cos \theta) f(\hat{\mathbf{u}}) d\hat{\mathbf{u}}, \quad (8.15)$$

where  $\hat{\mathbf{u}}$  is an orientational unit vector, and  $\mathcal{P}_2$  is the second Legendre polynomial. For a dispersion of isotropic rods  $S = 0$ , whereas for ordered phases  $S$  can attain larger values, approaching  $S \rightarrow 1$  for highly ordered rods. For the nematic phase of infinitely long rods considered here,

$$S = 4\pi \int_0^{\pi/2} f(\theta) \left[ \frac{3}{2} \cos^2 \theta - \frac{1}{2} \right] \sin(\theta) d\theta \quad (8.16)$$

has the value

$$S = 0.7922 \quad (8.17)$$

for the coexisting nematic phase.

More convenient calculations of the phase transition can be performed by choosing a trial function for the orientational distribution function  $f$  with one or more variational parameters. The free energy as a function of these parameters can then be minimised with respect to these parameters. Onsager [30] chose the following function:

$$f_{\text{O}}(\theta) = \frac{\kappa \cosh(\kappa \cos \theta)}{4\pi \sinh \kappa}. \quad (8.18)$$

This expression only has a single variational parameter ( $\kappa$ ) and gives the following results for the coexisting concentrations and nematic order parameter at coexistence:

$$c_{\text{I}} = 3.340, \quad c_{\text{N}} = 4.486, \quad S = 0.848. \quad (8.19)$$

Comparison of these results with the exact values in Eqs. (8.14) and (8.17) shows that the trial function chosen by Onsager works quite well.

Odijk [35,36] realised that for large values of  $\kappa$  (and thus, for highly ordered nematics), Onsager's orientational distribution function can be approximated by a simple Gaussian distribution function:

$$f_{\text{G}} \sim \tilde{N}(\kappa) \exp\left(-\frac{1}{2}\kappa\theta^2\right) \quad 0 \leq \theta \leq \frac{\pi}{2}, \quad (8.20a)$$

$$\sim \tilde{N}(\kappa) \exp\left(-\frac{1}{2}\kappa(\pi - \theta)^2\right) \quad \frac{\pi}{2} \leq \theta \leq \pi. \quad (8.20b)$$

where  $\tilde{N}(\kappa)$  is a normalisation constant. The advantage of this Gaussian distribution function is that for large values of  $\kappa$  the quantities  $\mathfrak{s}[f]$  and  $\rho[f]$  can be represented by the analytic expressions

$$\mathfrak{s}[f_{\text{G}}] \sim \ln \kappa - 1, \quad (8.21)$$

and

$$\rho[f_{\text{G}}] \sim \frac{4}{\sqrt{\pi\kappa}}. \quad (8.22)$$

This leads to the following expression for the free energy in the nematic phase:

$$\frac{F}{NkT} \sim \text{constant} - 1 + \ln c + \ln \kappa - 1 + \frac{4c}{\sqrt{\pi\kappa}}. \quad (8.23)$$

Minimising this expression with respect to  $\kappa$ ,

$$\frac{\partial F}{\partial \kappa} = 0, \quad (8.24)$$

leads to

$$\kappa \sim \frac{4c^2}{\pi}. \quad (8.25)$$

Hence,

$$\frac{F}{NkT} \sim \text{constant} + \ln \frac{4}{\pi} + 3 \ln c. \quad (8.26)$$

Applying Eqs. (8.11a) and (8.11b) yields the following results for the (osmotic) pressure and chemical potential of the rods in the nematic phase:

$$\frac{P_{\text{N}}b}{kT} = 3c_{\text{N}}, \quad (8.27a)$$

$$\frac{\mu_{\text{N}}}{kT} = \text{constant} + \ln \frac{4}{\pi} + 3 + 3 \ln c_{\text{N}}. \quad (8.27b)$$

Combining these with the expressions given by Eqs. (8.12a) and (8.12b) for the pressure and chemical potential in the isotropic phase, the coexistence Eqs. (8.10a) and (8.10b) now take the simple forms:

$$c_{\text{I}} + c_{\text{I}}^2 = 3c_{\text{N}} \quad (8.28a)$$

$$\ln c_{\text{I}} + 2c_{\text{I}} = 3 \ln c_{\text{N}} + \ln \left( \frac{4}{\pi} \right) + 3 \quad (8.28b)$$

From this, we find the following coexisting concentrations:

$$c_{\text{I}} = 3.451, \quad c_{\text{N}} = 5.122, \quad (8.29)$$

implying, via Eq. (8.25), that  $\kappa = 33.4$ . Insertion of Eqs. (8.20a) and (8.20b) into Eq. (8.16) using this value for  $\kappa$  gives

$$S = 0.910 \quad (8.30)$$

for the nematic order parameter in the coexisting nematic phase.

While the results for the Gaussian distribution function differ more from the exact results than the Onsager trial function (although in both cases the values are too high for the coexisting concentrations and for the order parameter in the coexisting nematic

phase), the calculations are substantially simpler [37] and provide a good estimate of the I–N transition in more complicated situations (that we will encounter in the next sections). Although the results of Onsager’s theory are of great fundamental and methodological interest, they refer strictly to infinitely thin hard rods. Hence, the applicability of the theory to experimental results is limited. In real suspensions of rod-like particles, we have to take into account one or more of the following aspects:

- particles are not infinitely thin,
- particles may be polydisperse in size,
- particles are not hard but may show (long-range) repulsions, for instance, due to charges or anchored polymeric brushes,
- there may be attractions between the particles and
- particles may be semiflexible.

Onsager [30] already addressed the issues of additional particle repulsions and polydispersity. These and the other issues raised above have been considered extensively (for a review, see [31]). Some of these complex elements will be treated in the rest of this chapter.

### 8.2.2 Charged Rods

In experimental systems, the rod-like particles are often charged. This means that, besides the hard-core excluded volume interaction, there is a double layer repulsion between the rods that gives rise to a soft repulsive interaction. Double layer forces between charged colloids in a polar solvent are specified by the range and the strength of the repulsive interaction [38]. The density of surface charge groups, which is directly related to the electrostatic surface potential  $\Psi$  at the rod surface, determines the strength of the repulsion. The ionic strength of the medium dictates the Debye length, which mediates the range of the double layer repulsion. Onsager [30] proposed to describe charged rods as hard rods with an *effective* diameter  $D_{\text{eff}} > D$ .

Stroobants, Lekkerkerker and Odijk [39] used the pair interaction between two charged rods to compute the second virial coefficient. This revealed an effective rod diameter that is given by

$$\frac{D_{\text{eff}}}{D} = 1 + \frac{\ln A' + k_E + \ln 2 - \frac{1}{2}}{D/\lambda_D}, \quad (8.31)$$

where  $\lambda_D$  is the ionic strength-dependent Debye length (see Sect. 1.2.2),  $k_E$  is Euler’s constant  $\approx 0.577$  and  $A'$  follows from the pair interaction as

$$A' = \frac{\pi \lambda_D \zeta^2 \exp[-D/\lambda_D]}{2\lambda_B}, \quad (8.32)$$

with  $\lambda_B$  the Bjerrum length (see Sect. 1.2.2). The parameter  $\zeta$  is the proportionality constant of the outer part of the double layer electrostatic potential profile near a charged rod [40]:

$$\frac{e\Psi(r)}{k_B T} \sim \zeta K_0(r/\lambda_D), \quad (8.33)$$

where  $e$  denotes the elementary charge,  $r$  represents the distance from the centre line of the rod, and  $K_0$  is the modified Bessel function of the second kind of order 0. For a weakly charged rod, the Debye–Hückel approximation provides [41]

$$\frac{e\Psi_{\text{DH}}(r)}{k_B T} = \frac{4Z\lambda_D\lambda_B K_0(r/\lambda_D)}{DK_1(D/2\lambda_D)}, \quad (8.34)$$

where  $Z$  is the linear charge density (per unit length) of the rod and  $K_1$  is the modified Bessel function of the second kind of order 1. Comparison of Eqs. (8.33) and (8.34) enables  $\zeta$  to be expressed in Eq. (8.32), giving

$$A'_{\text{DH}} = \frac{8\pi Z^2 \lambda_D^3 \lambda_B \exp[-D/\lambda_D]}{D^2 K_1^2(D/2\lambda_D)}. \quad (8.35)$$

For thick and thin double layers, this results in the following respective asymptotic analytical results [31]:

$$A'_{\text{DH}} \simeq \begin{cases} 2\pi Z^2 \lambda_D \lambda_B & D \ll \lambda_D, \\ \frac{8Z^2 \lambda_D^2 \lambda_B}{D} & D \gg \lambda_D. \end{cases} \quad (8.36)$$

Insertion of  $D_{\text{eff}}$  for  $D$  into the equations for hard rods then enables the physical properties of charged rods to be predicted. One may, for instance, insert the effective rod concentration given in Eq. (8.2) using  $D_{\text{eff}}$  to quantify the isotropic–nematic phase transition of long thin rods outlined in the previous section. It is noted that electrostatic twisting effects are not accounted for here. For those interested, see, for instance, Ref. [39].

---

### 8.3 Scaled Particle Theory of the Isotropic–Nematic Transition

When considering finite-sized rods (and later on, the effect of depletion attraction on the I–N transition in rod-like suspensions), we must take into account that the second virial term  $B_2$  no longer strongly exceeds the higher virial terms. When there are attractions between the rods, nearly parallel configurations are of paramount importance and  $B_2$  is no longer the dominating virial coefficient, as in the case of long, repulsive rods. It was shown that, for even slightly attractive rods, the third virial coefficient  $B_3$  is almost as large as  $B_2$  [42]. This means that we must start from a theory that takes into account higher virial coefficients. Here, we use scaled particle theory (SPT) [43], which will be treated in this section. SPT for rods mixed with polymers will subsequently be addressed in Sect. 8.4, following [44, 45].

SPT—a convenient and tractable way to incorporate higher virial coefficients in the treatment of the isotropic–nematic phase transition—was applied in Sect. 7.3 to obtain the osmotic pressure of an isotropic suspension of rods. The starting point of SPT is the calculation of the reversible work  $W$  to insert an additional spherocylinder into the system of spherocylinders to obtain the excess part of the chemical potential:

$$\mu^{\text{ex}} = \int f(\mathbf{\Omega}) W(\mathbf{\Omega}, 1, 1) d\mathbf{\Omega}, \quad (8.37)$$

where  $W(\mathbf{\Omega}, 1, 1)$  is the reversible work to insert a spherocylinder with length  $L$  and diameter  $D$  and orientation  $\mathbf{\Omega}$  in a system of hard spherocylinders. In Sect. 7.3, we considered an isotropic assembly of rods but Eq. (8.37) applies equally well to an orientationally ordered (nematic) system of rods, as long as we use an accurate expression for the orientation distribution function,  $f(\mathbf{\Omega})$ . After replacing the second virial contribution  $2c\rho[f]$  in Eq. (8.13b) with the chemical potential  $\mu^{\text{ex}}$ , we obtain

$$\begin{aligned} \frac{\mu}{kT} = \text{constant}' + \ln y + \mathfrak{s}[f], \\ + (1 + 2A[f])y + \left( A[f] + \frac{3}{2}B[f] \right) y^2 + B[f]y^3. \end{aligned} \quad (8.38)$$

Here,  $y$  has its usual meaning

$$y = \frac{\phi}{1 - \phi},$$

with  $\phi$  the volume fraction of the rods (which equals  $nv_0$ ), and  $v_0$  as the spherocylinder volume given by

$$v_0 = \frac{\pi}{4}LD^2 + \frac{\pi}{6}D^3.$$

The quantities  $A[f]$  and  $B[f]$  are defined as

$$A[f] = 3 + \frac{3(\Gamma - 1)^2}{3\Gamma - 1}\rho[f] \quad (8.39)$$

$$B[f] = \frac{12\Gamma(2\Gamma - 1)}{(3\Gamma - 1)^2} + \frac{12\Gamma(\Gamma - 1)^2}{(3\Gamma - 1)^2}\rho[f], \quad (8.40)$$

where

$$\Gamma = \frac{L}{D} + 1 \quad (8.41)$$

is the overall length-to-diameter ratio. Using the Gibbs–Duhem equation (see Eq. (A.12)), one obtains for the pressure

$$\frac{Pv_0}{kT} = y + A[f]y^2 + B[f]y^3 \quad (8.42)$$

---

**Exercise 8.3.** Show that Eq. (8.42) recovers the SPT expression for the pressure of a hard-sphere fluid (Eq. (3.37)) by setting  $\Gamma = 1$  and imposing Eq. (8.7).

---

Finally, the Helmholtz energy can be obtained from the relation

$$F = N\mu - PV,$$

leading to

$$\frac{F[f]}{NkT} = \frac{\tilde{F}[f]}{\phi} = \text{constant}' - 1 + \mathfrak{s}[f] + \ln y + A[f]y + \frac{1}{2}B[f]y^2, \quad (8.43)$$

with  $\tilde{F} = Fv_0/kTV$  (see Appendix A.2), which will be used in later sections.

---

**Exercise 8.4.** Show that in the limit  $L/D \rightarrow \infty$  and low concentrations the above expression for the free energy reduces to the free energy in the second virial approximation Eq. (8.1) with  $\text{constant}' = \text{constant} + \ln(L/D)$ .

---

As indicated earlier, the I–N phase equilibria can be found simultaneously:

- using Eq. (8.24) to minimise  $F[f]$  numerically with respect to the orientational distribution function  $f$ ,
- calculating the orientation distribution function of  $f$ ,
- calculating the (osmotic) pressure and chemical potential and
- solving the coexistence equations.

Hence, there are three equations with three unknowns: the two coexistence concentrations and  $\kappa$ . The results for the coexisting concentrations, which now depend on  $L/D$ , are given in Fig. 8.4 (see also [45]). In this figure, we also present Monte Carlo simulation results [27] and the Onsager limit result ( $L/D \rightarrow \infty$ ). Clearly, the agreement between numerically solving the SPT expressions (solid curves) and computer simulation results is quite good. In Fig. 8.5, we give the coexistence pressure at isotropic–nematic coexistence for hard spherocylinders as a function of the aspect ratio  $L/D$ .

It is interesting to compare the results obtained with the numerical orientational distribution function with the results obtained with the Gaussian orientational distribution function Eqs. (8.20a) and (8.20b). Minimising the free energy of Eq. (8.43) is possible by substituting the expressions for  $\mathfrak{s}[f_G]$  and  $\rho[f_G]$  that are given by Eqs. (8.21) and (8.22). This yields the following expression for  $\kappa$ :

$$\kappa = \frac{36}{\pi} \frac{(\Gamma - 1)^4}{(3\Gamma - 1)^2} \left( y + \frac{2\Gamma}{3\Gamma - 1} y^2 \right)^2. \quad (8.44)$$

**Fig. 8.4** Isotropic–nematic phase coexistence for hard spherocylinders as a function of the inverse of the aspect ratio  $L/D$

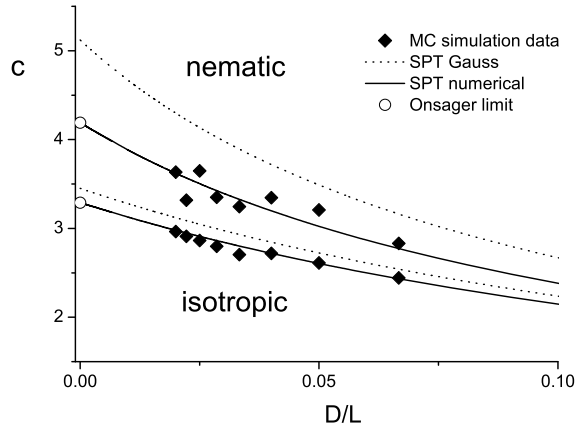
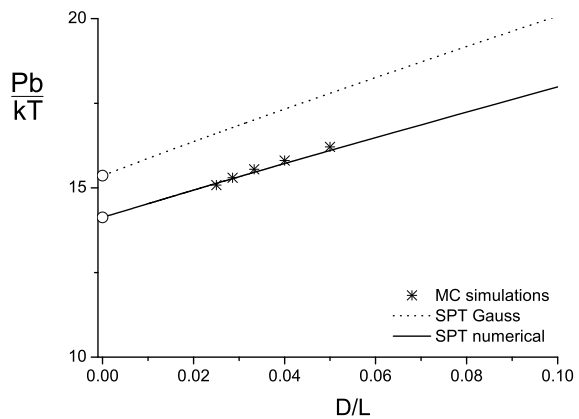


**Fig. 8.5** Pressure  $Pb/kT$  at isotropic–nematic coexistence for hard spherocylinders as a function of  $D/L$ . Note  $v_0 = b[D/L + (2/3)(D/L)^2]$



**Exercise 8.5.** Show that in the limit  $L/D \rightarrow \infty$  and at low rod concentrations Eq. (8.44) reduces to Eq. (8.25).

Using Eq. (8.44) for  $\kappa$  in  $\mathfrak{s}[f_G]$  and  $\rho[f_G]$ , and substituting these expressions in Eqs. (8.38) and (8.42), provides us with analytical expressions for the chemical potential and pressure in the nematic phase. The expressions for these quantities in the isotropic phase are obtained by setting  $\mathfrak{s} = 0$  and  $\rho = 1$  in equations (8.38) – (8.42). We can then solve the coexistence equations (8.10a) and (8.10b). The results for the coexisting concentrations and the coexistence pressure obtained using the Gaussian orientational distribution function are also given in Figs. 8.4 and 8.5 as the dashed curves.

As in the Onsager limit, the results lie somewhat above the numerical solution but are still quite reasonable. Given the fact that the Gaussian approximation is transparent and simple, its use provides an extremely valuable method to scan through a large parameter space as we shall see in the next sections.

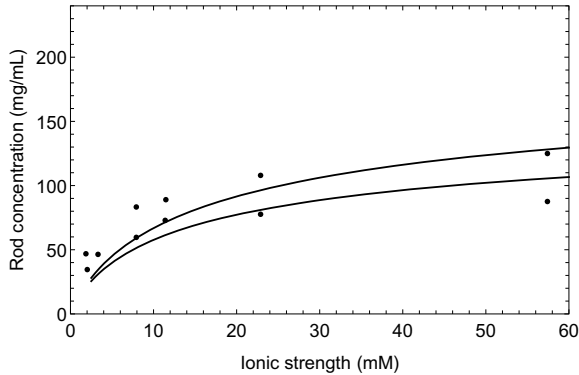


**Fig. 8.6** Isotropic–nematic phase transition concentrations of TMV as a function of the ionic strength. The data points are experimental results redrawn from Ref. [46]. Curves represent SPT with  $D_{\text{eff}}$  calculated by using Eq. (8.31) and following [39]. Equation (8.35) was used to calculate  $A'$ . Parameters used:  $L = 282$  nm,  $D = 18$  nm, charge density  $Z = -10$  e/nm and virus particle molar mass  $M_p = 4 \cdot 10^7$  g/mol

This SPT description can be extended to also include the influence of a double layer surrounding the rods in a polar solvent due to charges at the rod surface. Basically, one can still apply Eq. (8.43) with Eq. (8.44) to describe charged rods, but  $D$  is instead replaced with  $D_{\text{eff}}$  given by Eq. (8.31). The I–N phase transition concentrations for TMV virus as a function of salt concentration are given in Fig. 8.6, as measured by Fraden et al. [46]. As the ionic strength increases the concentration of virus in the coexisting phases increases. Without added salt, an isotropic phase of 15 mg/mL TMV coexists with a nematic phase of 23 mg/mL, while, at an ionic strength of 60 mM, the coexisting concentrations are 90 mg/mL in the isotropic phase and 125 mg/mL in the nematic phase. Replacing the electrostatic potential between TMV particles with an appropriate effective diameter gives a reasonably good description of the experimentally observed phase boundaries [46]. This provides information on how the I–N phase coexistence varies with  $D_{\text{eff}}$ , which in turn depends on the ionic strength for charged rods.

## 8.4 Isotropic–Nematic Phase Behaviour of Rods Mixed with Penetrable Hard Spheres

We now consider the effect of added polymer on the phase behaviour of a system of hard rods. The simplest representation of a polymer is a penetrable hard sphere (PHS) with diameter  $\sigma = 2\delta$  and radius  $\delta$  equal to the depletion thickness. See Sect. 2.1 for details about the PHS model.

The starting point for the calculation of the phase behaviour is the semi-grand potential for the colloidal rods–PHSs system that is in osmotic equilibrium with a reservoir of PHSs, which sets the chemical potential of the PHSs. This system is depicted in Fig. 8.7. In the free volume approximation (see Sect. 3.3), we can write

**Fig. 8.7** Osmotic equilibrium between a dispersion of hard rods and penetrable hard spheres (the system) and a reservoir containing a penetrable hard-sphere dispersion

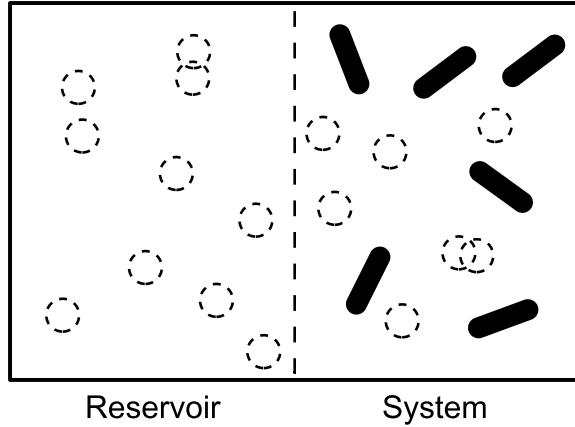
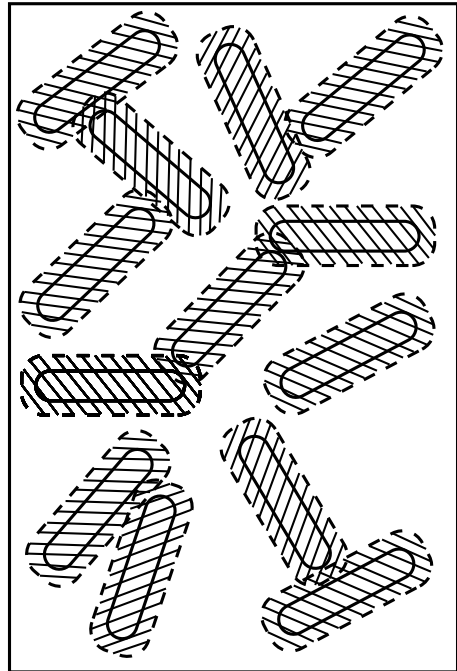


**Fig. 8.8** Illustration of the available free volume (the unshaded volume) in a dispersion of hard spherocylinders



Eq. (3.26) as

$$\Omega(N_1, V, T, \mu_2) = F_0(N_1, V, T) - P^R \langle V_{\text{free}} \rangle_0, \quad (8.45)$$

where  $N_1$  stands for the number of rods,  $\mu_2$  represents the chemical potential of the depletants (PHSs),  $P^R$  is the pressure in the reservoir and  $\langle V_{\text{free}} \rangle_0$  is the free volume for PHSs in the system of rods, illustrated in Fig. 8.8.

For  $F(N_1, V, T)$ , we use the SPT expression (Eq. (8.43)) [43], and the osmotic pressure of the PHSs in the reservoir is given by

$$P^R = n_2^R kT,$$

where  $n_2^R$  is the number density of PHSs in the reservoir. The free volume is again calculated using the relation

$$\frac{\langle V_{\text{free}} \rangle_0}{V} = \alpha = e^{-W/kT}, \quad (8.46)$$

where  $W$  is the reversible work for inserting the PHSs into the hard rod suspension. An expression for the work of insertion  $W$  can again be conveniently obtained using SPT. The work  $W$  is calculated by expanding the PHS to be inserted from zero to its final size. By writing the size of the scaled PHS as  $\lambda\sigma$  ( $= 2\lambda\delta$ ) in the limit that  $\lambda \rightarrow 0$ , the inserted sphere approaches a point particle. In this limit, it is very unlikely that excluded volumes of the hard rods and added scaled PHS overlap. So,

$$W(\lambda) = -kT \ln [1 - n_1 v_{\text{excl}}(\lambda)] \quad \text{for } \lambda \ll 1, \quad (8.47)$$

where  $v_{\text{excl}}(\lambda)$  is the excluded volume of the added scaled PHS and a hard spherocylinder with length  $L$  and diameter  $D$ :

$$v_{\text{excl}}(\lambda) = \frac{\pi}{4}(D + \lambda\sigma)^2 L + \frac{\pi}{6}(D + \lambda\sigma)^3. \quad (8.48)$$

The opposite limit  $\lambda \gg 1$  corresponds to the case when the size of the inserted PHS is very large. Then  $W$  is, to a good approximation, equal to the volume work needed to create a cavity with volume

$$\frac{\pi}{6}(\lambda\sigma)^3$$

and is given by

$$W = \frac{\pi}{6}(\lambda\sigma)^3 P \quad \text{for } \lambda \gg 1, \quad (8.49)$$

where  $P$  is the (osmotic) pressure of the hard rod system given by (Eq. (8.42)).

In SPT, the above two limiting cases are connected by expanding  $W$  in a series in  $\lambda$ :

$$W(\lambda) = W(0) + \left( \frac{\partial W}{\partial \lambda} \right)_{\lambda=0} \lambda + \frac{1}{2} \left( \frac{\partial^2 W}{\partial \lambda^2} \right)_{\lambda=0} \lambda^2 + \frac{\pi}{6}(\lambda\sigma)^3 P. \quad (8.50)$$

This yields

$$\begin{aligned} \frac{W(\lambda=1)}{kT} = & -\ln(1 - \phi_1) + \left[ \frac{6\Gamma q}{3\Gamma - 1} + \frac{3(\Gamma + 1)q^2}{3\Gamma - 1} \right] y_1 \\ & + \frac{1}{2} \left( \frac{6\Gamma}{3\Gamma - 1} \right)^2 q^2 y_1^2 + \frac{2q^3}{3\Gamma - 1} \frac{Pv_0}{kT}, \end{aligned} \quad (8.51)$$

where

$$y_1 = \frac{\phi_1}{1 - \phi_1}$$

$$q = \frac{\sigma}{D} = \frac{2\delta}{D}$$

Inserting (Eq. (8.42)) for the pressure  $P$  of spherocylinders leads to the following expression for the free volume fraction:

$$\alpha = (1 - \phi_1) \exp[-Q(\phi_1)], \quad (8.52)$$

where

$$Q(\phi_1) = ay_1 + by_1^2 + cy_1^3 \quad (8.53)$$

with

$$a = \frac{6\Gamma}{3\Gamma - 1}q + \frac{3(\Gamma + 1)}{3\Gamma - 1}q^2 + \frac{2}{3\Gamma - 1}q^3, \quad (8.54a)$$

$$b = \frac{1}{2} \left( \frac{6\Gamma}{3\Gamma - 1} \right)^2 q^2 + \left( \frac{6}{3\Gamma - 1} + \frac{6(\Gamma - 1)^2}{(3\Gamma - 1)^2} \rho[f] \right) q^3, \quad (8.54b)$$

$$c = \frac{2}{3\Gamma - 1} \left( \frac{12\Gamma(2\Gamma - 1)}{(3\Gamma - 1)^2} + \frac{12\Gamma(\Gamma - 1)^2}{(3\Gamma - 1)^2} \rho[f] \right) q^3. \quad (8.54c)$$

---

**Exercise 8.6.** Check that, in the appropriate limit, Eq. (8.52) with Eqs. (8.53) and (8.54),  $\alpha$  reduces to Eq. (3.38) with  $a$ ,  $b$  and  $c$  given by Eq. (3.38).

---

We now have all the contributions to construct the semi-grand potential  $\Omega$  given in (Eq. (8.45)). In order to obtain the phase behaviour, we proceed along the same lines as for the system of pure rods involving the following steps:

- minimise  $\Omega$  with respect to the orientation distribution function  $f$  (compute the value of  $\kappa$  at which  $\partial\Omega/\partial\kappa = 0$ ). Note that, in Eq. (8.45), both the free energy of the pure rod system  $F_0$  and the free volume  $\langle V_{\text{free}} \rangle_0$  depend on the orientation distribution function  $f$
- evaluate the orientation distribution function  $f$
- calculate the (osmotic) pressure and chemical potential of the rods, which are given by

$$P = - \left( \frac{\partial \Omega}{\partial V} \right)_{N_1, \mu_2} = P^0 + P^R \left( \alpha - n_1 \frac{d\alpha}{dn_1} \right), \quad (8.55)$$

$$\mu_1 = \left( \frac{\partial \Omega}{\partial N_1} \right)_{V, \mu_2} = \mu_1^0 - P^R \frac{d\alpha}{dn_1}, \quad (8.56)$$

where  $P^0$  and  $\mu^0$  are the pressure and chemical potential of the pure rod system, and

- solve the coexistence relations (Eqs. (A.13) and (A.14))

$$\mu_1^I(n_1^I, \mu_2) = \mu_1^{II}(n_1^{II}, \mu_2), \quad (8.57)$$

$$P^I(n_1^I, \mu_2) = P^{II}(n_1^{II}, \mu_2). \quad (8.58)$$

Instead of formal minimisation of the free energy leading to an integral equation for the orientational distribution function  $f$ , we will first use the Gaussian distribution function, which simplifies the calculations considerably while leading to reasonably accurate results. This is illustrated in Fig. 8.9, where we plot the isotropic–nematic phase coexistence curve for  $L/D = 10$  and  $q = 1$ . On the ordinate, the relative reservoir concentration of PHSs in the reservoir  $\phi_2^R$  is plotted versus the volume fraction of hard spherocylinders on the abscissa. The solid curves are the results for the binodals using the Gaussian distribution function, while the dashed curves were obtained using formal minimisation (see Ref. [45]). In Fig. 8.4, it was demonstrated that the Gaussian overestimates the I–N concentrations somewhat for the pure hard

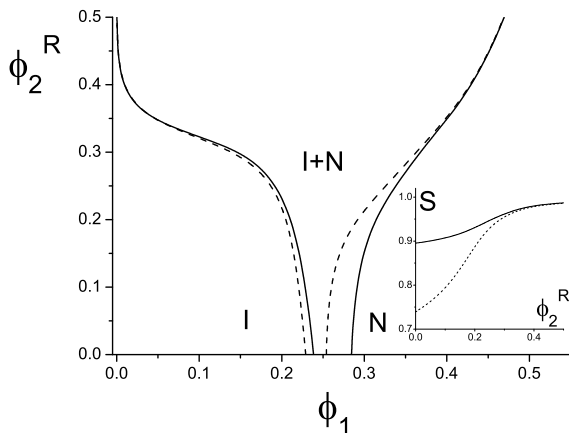


**Fig. 8.9** Isotropic–nematic phase coexistence for  $L/D = 10$  and  $q = 1$  in the reservoir representation. The Gaussian orientational distribution function result (solid curves) is compared to the coexistence computed using formal minimisation of the oriental distribution function (dashed curves). *Inset:* Plot of the nematic order parameter  $S$  as a function of  $\phi_2^R$  of the nematic phase (numerical approach: dotted curve, Gaussian approximation: solid curve) that coexists with the isotropic phase

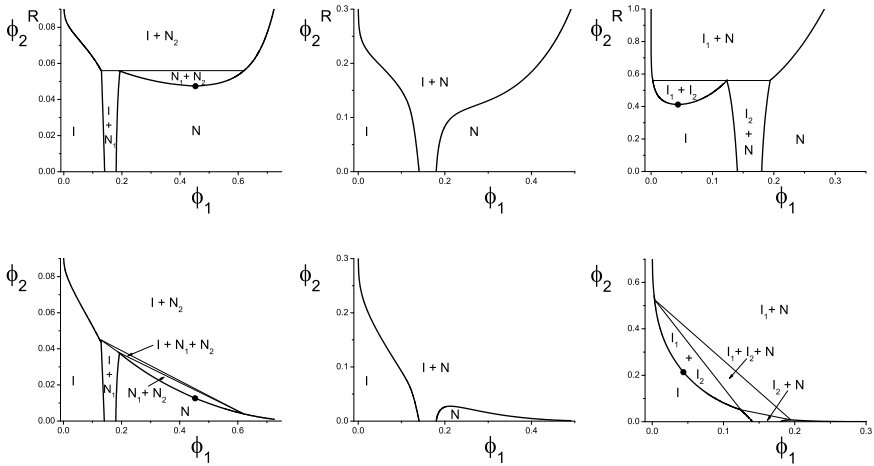


**Fig. 8.10** Phase diagrams calculated using free volume theory for spherocylinders ( $L/D = 20$ ) with added PHSs at three size ratios:  $q = 0.3$  (left),  $q = 1$  (middle) and  $q = 2.5$  (right). The upper three curves are in the reservoir representation and the lower curves are the system results. The Gaussian form for the ODF was used to minimise the semi-grand potential and compute the coexistence concentrations

spherocylinder dispersion, which is also shown here. For a pure rod dispersion the Gaussian approximation provides a too sharply peaked orientation distribution function  $f$ , reflected by a too large value for the nematic order parameter  $S$ . Hence, the loss of orientational entropy is overestimated for the pure rod dispersion.

As the depletant concentration becomes significant and attractions play a dominating role  $f$  becomes sharply peaked. This is reflected in a strong increase of the nematic order parameter  $S$  (see the inset in Fig. 8.9). Hence, the Gaussian orientational distribution function becomes increasingly accurate at larger depletant concentrations.

Phase diagrams for  $L/D = 20$ , computed using the Gaussian  $f$ , are plotted in Fig. 8.10 for  $q = 0.3$ ,  $q = 1$  and  $q = 2.5$ . The upper plots are the reservoir depletant–rod representations, while the lower plots are the system representations. These three size ratios reflect different scenarios that are found in mixtures of spherocylinders and depletants when accounting for rods in the isotropic and/or nematic phase states. Depending on the length-to-width ratio of the rod-like particles and the ratio of the depletant diameter over the rod diameter, we find the following types of phase equilibria:

- coexistence between two isotropic phases (dilute and concentrated are the equivalent of vapour and liquid) and a nematic phase. This phase behaviour is predicted to occur for mixtures of relatively short rods and large depletants, so long-ranged attractions.
- coexistence between an isotropic and a nematic phase.
- equilibria between two coexisting nematic phases for rods mixed with small depletants, so short-ranged attractions.

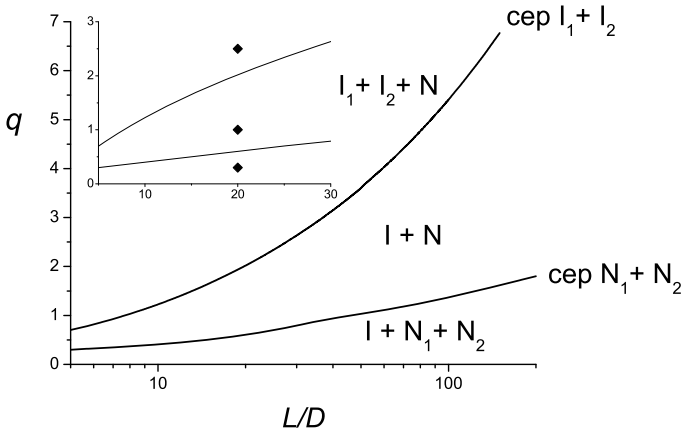


**Fig. 8.11** Critical end point (cep) curves for isotropic–isotropic ( $I_1$ – $I_2$ ) and nematic–nematic ( $N_1$ – $N_2$ ) coexistence in dispersions of hard spherocylinders and PHSs as a function of the aspect ratio  $L/D$ . Computed using the Gaussian approximation for the orientational distribution function. *Inset*: magnified region for relatively small  $L/D$

- coexistence between one isotropic phase and two nematic phases differing in concentration. This phase behaviour is predicted to occur for long rod-like particles and relatively small depletants.

A critical end point (CEP) exists for both the critical isotropic–isotropic and nematic–nematic points at given  $L/D$ . This CEP identifies the conditions for which a certain phase transition ceases to exist. The occurrence of the three different regimes as a function of the geometrical parameters  $L/D$  and  $q$  is shown in Fig. 8.11, as marked by the isotropic–isotropic and nematic–nematic critical end points. As a function of  $L/D$  the CEP values provide critical end curves. In the inset of Fig. 8.11, we have marked the conditions for which we plotted the phase diagrams in Fig. 8.10.

The three types of phase behaviour are illustrated in Fig. 8.10 in a representation showing colloid volume fraction  $\phi_1$  against depletant concentration  $\phi_2^R$ . Experimentally, one controls the depletant (for instance, nonadsorbing polymer) concentration in the system:

$$n_2 = -\frac{1}{V} \left( \frac{\partial \Omega}{\partial \mu_2} \right)_{N_2, V}, \tag{8.59}$$

rather than the polymer concentration (chemical potential) in the reservoir. Using the relation

$$\alpha = \frac{n_2}{n_2^R} = \frac{\phi_2}{\phi_2^R}, \tag{8.60}$$

phase diagrams in the experimentally accessible  $(\phi_1, \phi_2)$  plane can be obtained from the results in the  $(\phi_1, \phi_2^R)$  plane. The resulting phase diagrams are presented in Fig. 8.10 (lower diagrams).

## 8.5 Experimental Phase Behaviour of Rod–Polymer Mixtures

In this section, experimental results on the isotropic–nematic transition in mixed suspensions of colloidal rods and polymer are discussed and compared to the theory presented in the previous sections. The experimental results refer to three types of rod-like colloidal particles, which in suspension give rise to isotropic–nematic phase separation above a critical concentration:

- stiff and semiflexible virus particles,
- cellulose nanocrystals and
- colloidal boehmite ( $\gamma$ -AlOOH) rods.

In several experimental examples in this chapter, the rods are semiflexible. These are usually described using the worm-like chain model, (see, for instance, Refs. [47, 48]). In this model, the rod-like object has some flexibility by assuming a gradual change of the direction of the chain, which is in between the random walk character of a Gaussian chain and a rigid rod. This gradual change is described by assuming fluctuations in bond lengths and bond angles. In Fig. 8.12,  $\mathbf{u}(s)$  is the direction vector of the chain at position  $s$  along the contour of the chain, and  $\Delta s$  is the angle ( $\theta_P$ ) between two direction vectors that are a distance apart. The persistence length  $l_P$  follows from:

$$\langle \mathbf{u}(s) \cdot \mathbf{u}(s + \Delta s) \rangle = \langle \cos \theta_P(\Delta s) \rangle = \exp\left(-\frac{\Delta s}{l_P}\right). \quad (8.61)$$

It follows that  $l_P$  is the characteristic length scale, on which the direction vector  $\mathbf{u}$  of the chain varies.

The polymers added to the rod-like particles range from polysaccharides (heparin, chondroitin sulfate, dextran) to polyethylene oxide (PEO) and polystyrene (PS).

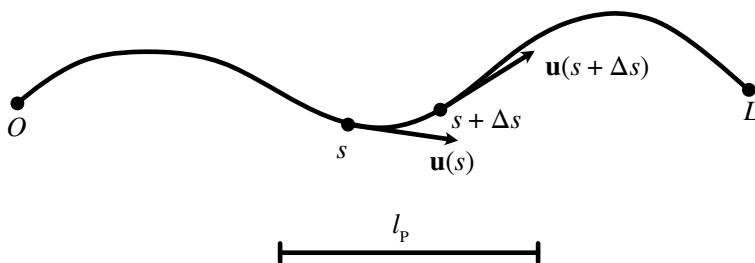


**Fig. 8.12** An example of a configuration of a semiflexible rod described as a worm-like chain starting at position  $O$ , having a length  $L$ . The quantity  $\mathbf{u}(s)$  is the direction vector of the chain at position  $s$ . For explanation of the other symbols, see the main text. Inspired by Fig. 8 in Ref. [31]

### 8.5.1 Stiff and Semiflexible Virus Particles Mixed with Polymer

Illustrative examples of rod-like colloidal particles are stiff and semiflexible virus particles, such as the plant virus tobacco mosaic virus (TMV) and the filamentous bacteriophages *fd*-virus, Pf1, Pf4. Table 8.1 summarises the characteristics of the virus particles discussed in this section.

Suspensions of TMV (see Fig. 8.13, taken from Ref. [56]) have long been recognised as an interesting system to study the I–N transition [4]. TMV is a rigid cylindrical particle consisting of a protein shell enclosing double-stranded RNA. Fraden et al. [46] measured the coexisting isotropic and nematic concentrations over a wide range of ionic strengths (Fig. 8.6).

It was as early as 1942 that Cohen [28] conducted a study directed at the isolation of TMV from infectious juice and observed that the addition of 5 mg/mL of the polysaccharide heparin to a dilute TMV suspension (2 mg/mL) in 0.1 M phosphate buffer (pH = 7.1) resulted in the production of needle-shaped paracrystals 5–20  $\mu\text{m}$  in length (see Fig. 1.11 in Ref. [28]). These crystals may be considered as precursors of the I–N transition [4]. In the 1990s, Sano and co-workers [56–58] added the polysaccharide chondroitin sulfate (Chs) to dilute TMV suspensions with a view to establish the antiviral activity of these polysaccharides. With electron microscopy, Urakami et al. [56] observed that the addition of very low concentrations of Chs (1 mg/mL) to dilute TMV suspensions (1 mg/mL) caused the formation of large raft-

**Table 8.1** Characteristics of TMV [46], (wild-type) *fd* [19,49–51], Pf1 [50,52,53] and Pf4 [54,55] virus particles. Acknowledgements to A. Tarafder, T. Bharat, P. Secor and P. Janmey for their help with compiling this table

Virus	$M_p$ (kDa)	$L$ ( $\mu\text{m}$ )	$D$ (nm)	$L/D$	$l_p$ ( $\mu\text{m}$ )
TMV	$4 \cdot 10^4$	0.3	18	17	$> 10L$
<i>fd</i>	$1.64 \cdot 10^4$	0.88	6.6	133	$2.5 \approx 2.8L$
Pf1	$3.5 \cdot 10^4$	2	6	333	$2 \approx L$
Pf4	$6.08 \cdot 10^4$	3.8	6	633	$2 \approx 0.5L$

**Fig. 8.13** TEM micrograph of TMV particles. Reprinted with permission from Ref. [56]. Copyright 1999 AIP Publishing

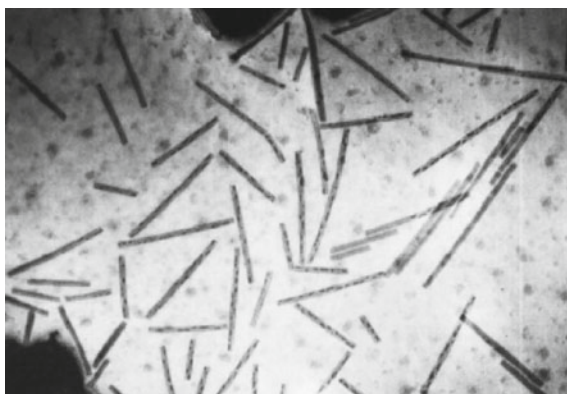


**Fig. 8.14** TEM micrograph of ordered TMV particles as induced by added chondroitin sulfate. Reprinted with permission from Ref. [56]. Copyright 1999 AIP Publishing

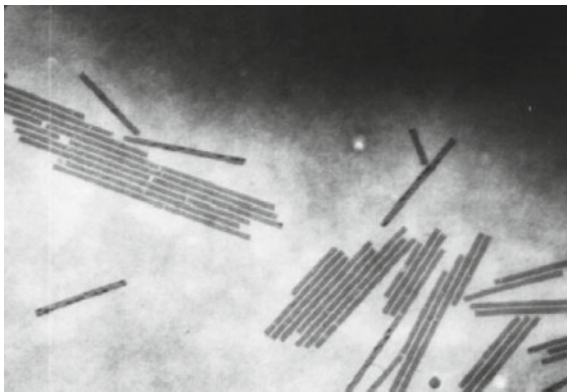
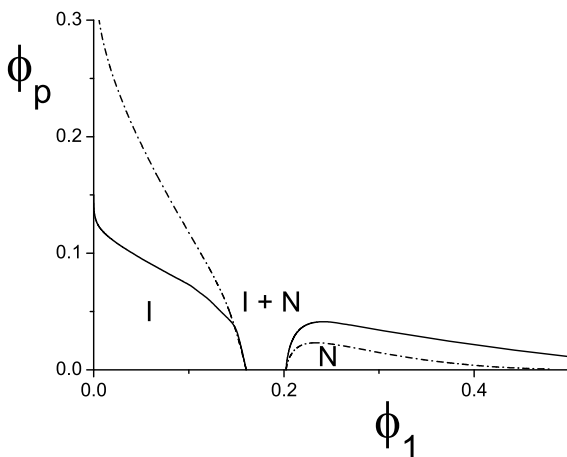


**Fig. 8.15** I–N phase coexistence for hard spherocylinders ( $L/D = 17$ ) mixed with PHSs, mimicking TMV mixed with polymers for size ratios  $q = 0.4$  (solid curves) and  $q = 1.1$  (dot-dashed curves)



like aggregates (Fig. 8.14). The effect of Chs on infectivity may, according to Sano [57], be ascribed to these raft-like aggregates blocking the decapsulation process of TMV protein on the cell membrane surface. The fact that very low Chs concentrations lead to aggregation of TMV is attributed to its semirigidity [56,58].

Leberman [29] observed that addition of 6 mg/mL of the flexible polymer polyethylene oxide (PEO) ( $M = 6$  kDa,  $R_g = 3.6$  nm) to a dilute 1 mg/mL TMV suspension leads to precipitation of TMV, which may be considered as a sign of the I–N transition. Figure 8.15 presents a comparison of this experimental observation with the theoretical phase diagram for  $L/D = 300/18 = 17$  and  $q = 2R_g/D = 2 \cdot 3.6/18 = 0.4$ , which are the relevant parameters for this mixed TMV–PEO suspension.

From this calculated phase diagram, we observe that at low TMV concentrations a relative polymer concentration  $\phi_p = 0.125$  is required to cause I–N phase separation, which corresponds in this case to a mass concentration of  $c_p = 3\phi_p M / 4\pi N_{Av} R_g^3 = 6.4$  mg/mL. The agreement with the experiment should be considered with care

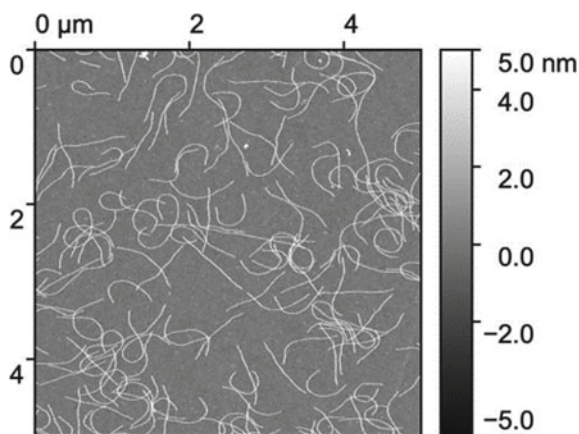
since the electrostatic interactions have not been taken into account in the theoretical calculation.

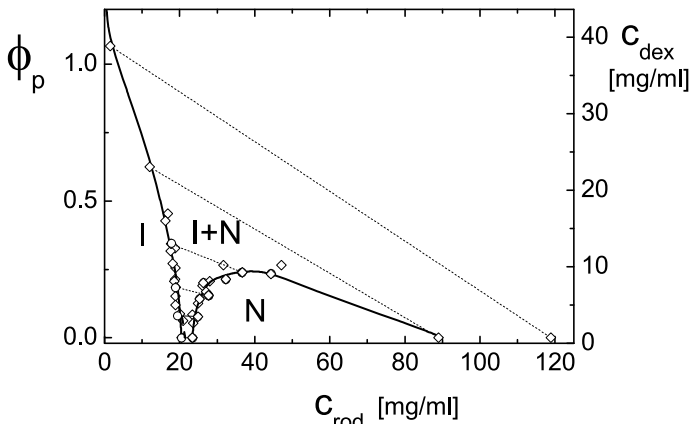
More extensive measurements on the I–N transition in TMV suspensions with added PEO ( $M = 100$  kDa,  $R_g = 10$  nm) were carried out by Adams and Fraden [49]. At TMV concentrations of 20 mg/mL (where the pure rod system is in the isotropic phase), they observed the first signs of I–N phase separation at 5 mg/mL added PEO and a more definite phase transition for 10 mg/mL added PEO. For a direct comparison with the experimental observation, Fig. 8.15 also presents the theoretical phase diagram for  $L/D = 17$  (TMV as before) but now with  $q = 2R_g/D = 2 \cdot 10/18 = 1.1$ , which are the relevant parameters for this mixed TMV–PEO suspension. From this calculated phase diagram, we observe that at low TMV concentration a relative polymer concentration  $\phi_p = 0.25$  is required to cause I–N phase separation, which corresponds in this case to a mass concentration of  $c_p = 3\phi_p M/4\pi N_{Av} R_g^3 = 10$  mg/mL. This is again in reasonable agreement with theory. As mentioned before, the electrostatic interactions that certainly play a role have not been taken into account, and therefore the comparison with experiment should be considered with care.

In addition to TMV, the liquid crystal phase behaviour of the semirigid cylindrical *fd*-virus has been investigated extensively. The *fd*-virus particle consists of a protein shell wound around a single ribbon of single-stranded DNA [59]. Figure 8.16 shows an AFM image of some *fd*-viruses. Near a neutral pH the linear charge density is  $-5$  to  $-20$  e/nm. Fraden and co-workers [50] measured the coexisting isotropic and (chiral) nematic concentrations over a wide range of ionic strengths of the wt *fd*-virus. The onset of the (chiral) nematic phase occurs from 10 to 20 mg/mL of *fd*-virus as the ionic strength is increased from 1 to 100 mM. Dogic et al. [60,61] studied the phase diagram of mixed suspensions of *fd* and dextran ( $M_p = 500$  kDa,  $R_g = 18$  nm) and an example is plotted in Fig. 8.17a.

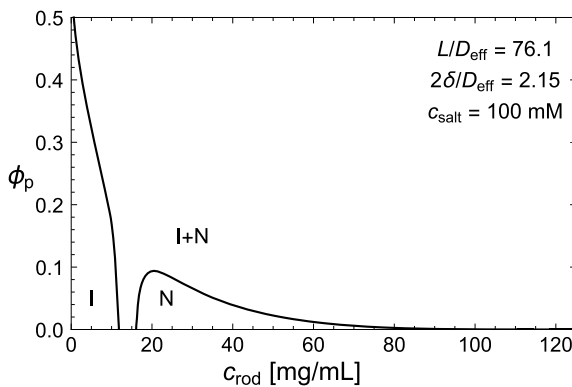
A clear widening of the I–N transition of the *fd*-virus rod dispersion takes place upon increasing the dextran concentration. Although this finding is quite general for the I–N binodal, the corresponding spinodal points related to this phase transi-

**Fig. 8.16** Image of *fd*-virus mutant type Y21M particles dried on a mica surface made using AFM. Scale and depth indicated. Image kindly provided by O. Deschaume, M.P. Lettinga and C. Bartic, KU Leuven, Belgium





(a)



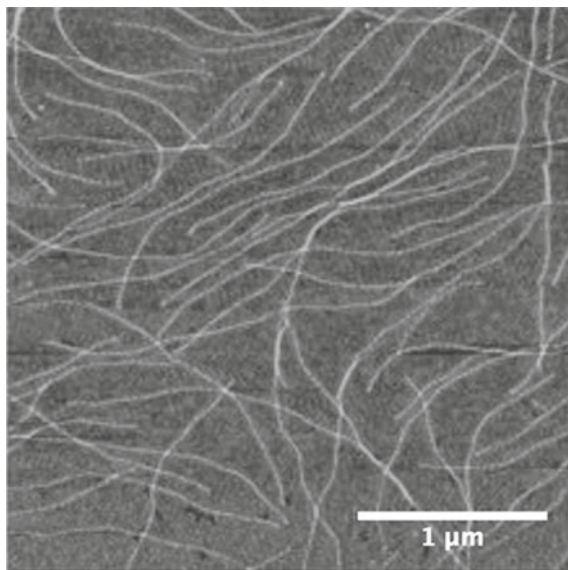
(b)

**Fig. 8.17** **a** Phase diagrams of dispersions containing *fd*-virus and dextran. Data points are measured phase coexistences. The phase diagram was measured at an ionic strength of 100 mM at pH = 8.15 with added 500 kDa dextrans. Data replotted from Ref. [61]. **b** Predicted I–N phase coexistence for spherocylinders ( $L/D = 133$ ,  $D_{\text{eff}} = 11.57$  nm,  $L/D_{\text{eff}} = 76.1$ , ionic strength of 100 mM) mixed with PHSs ( $2\delta/D_{\text{eff}} = 2.15$ ). The dextran polymer has  $R_g = 17.6$  nm and the charge density is taken as  $-10$  e/nm

tion seem to be much less affected by adding nonadsorbing polymers [62]. At low *fd*-virus concentrations, the I–N transition takes place upon adding large polymer concentrations.

For direct comparison with the experimental phase diagram, we present the theoretical phase diagram for  $L/D = 880/6.6 = 133$  and  $q = 2R_g/D = 2 \cdot 11/6.6 = 3.3$  in Fig. 8.17b. For detailed accounts of the ideal polymer chains, see Refs. [45,61]. The overall agreement between theory and experiment (compare Figs. 8.17a and 8.17b), while far from perfect, is satisfactory considering that *fd* is not completely rigid and that dextrans are branched polymers. The rod flexibility is known to have a significant effect on the I–N phase behaviour [31]. This is demonstrated by the inter-

**Fig. 8.18** Atomic force microscopy image of Pf1 viruses in monovalent salt. Image kindly provided by P.A. Janmey from their study reported in Ref. [64]



esting work of Barry, Beller and Dogic [63], who compared the phase behaviour of a mutant filamentous virus, *fd* Y21M (Fig. 8.16), to that of a conventional *fd* wt. The persistence length of *fd* wt is  $2.8 \pm 0.7 \mu\text{m}$ , whereas the persistence length of *fd* Y21M is  $9.9 \pm 1.6 \mu\text{m}$ . Compared to *fd* wt, the location of the isotropic–cholesteric phase transition for *fd* Y21M shifts to lower densities and approaches values that are remarkably close to the Onsager prediction for rigid rods.

The filamentous bacteriophages Pf1 [50,53,64] and Pf4 [54,55] are structurally similar to *fd*-virus. An atomic force microscopy image of the filamentous bacteriophage Pf1 [64] is presented in Fig. 8.18.

Booy and Fowler [65] observed small domains of smectic organisation (cybotactic clusters [2]) in a nematic phase in suspensions of Pf1 at a concentration of 40 mg/mL. Using optical microscopy Dogic and Fraden [50] observed coexisting regions of the nematic and smectic phases in suspensions of Pf1 with abrupt boundaries between the phases, which is evidence of a first-order phase transition.

So far, no liquid crystal phases in pure suspensions of Pf4 have been reported; but Secor et al. [54] and Tarafder et al. [55] observed liquid crystal tactoids in suspensions of Pf4 upon adding sodium alginate. In Fig. 8.19, we show the concentrations of Pf4 and sodium alginate where the tactoids appear [54].

Tarafder et al. [55] provided beautiful fluorescence microscopy images of Pf4 tactoids observed after mixing Pf4 with sodium alginate (Fig. 8.20a). The key role of the tactoids is that they can encapsulate the pathogenic bacterium *Pseudomonas aeruginosa*, shielding them from antibiotics [54,55,66]. Illustrative fluorescence microscopy images of this encapsulation (Fig. 8.20b), can be found in [55].

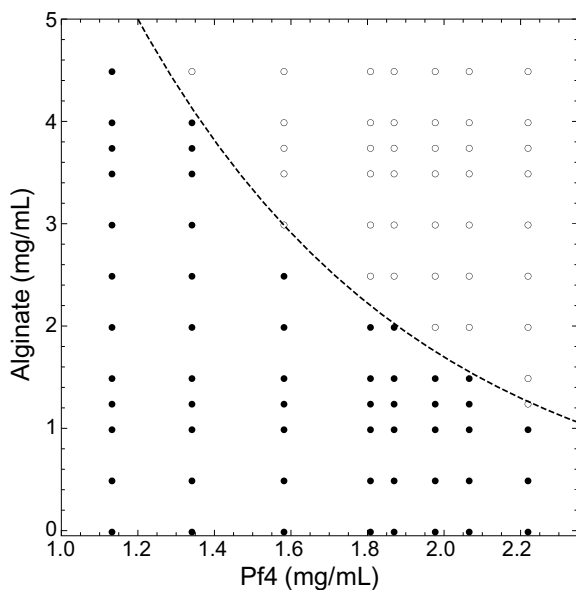


**Fig. 8.19** Phase diagram indicating the stable (one phase) region (closed symbols) and unstable demixing region (open symbols) in terms of the polymer (alginate) concentration and virus (Pf4) concentration. The dotted curve that indicates the phase transition concentrations is drawn to guide the eye. Replotted from the data in Ref. [54]

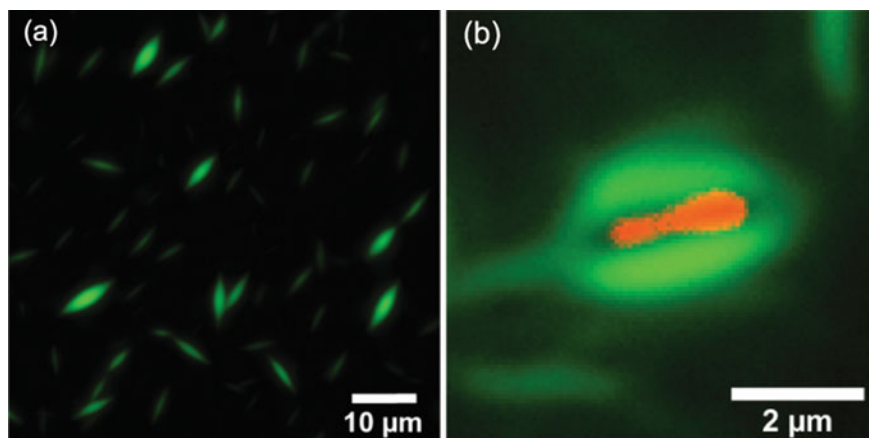


**Fig. 8.20** Fluorescence microscopy images of Pf4 tactoids. **a** Tactoids observed in a mixture of 1 mg/mL Pf4 and 10 mg/mL sodium alginate 24 h after mixing and **b** tactoids of Pf4 encapsulate *Pseudomonas Aeruginosa* [55]. Figures were kindly provided by A.K. Tarafder and T.A.M. Bharat

### 8.5.2 Cellulose Nanocrystals Mixed with Nonadsorbing Polymers

In 1959, Marchessault, Morehead and Walter [67] reported on the formation of liquid crystals in suspensions of cellulose nanocrystals prepared from cellulose by acid hydrolysis in sulfuric acid (see Fig. 8.1m for a microscopy image of cellulose nanorods). The study of the isotropic–(chiral) nematic phase transition in suspensions of cellulose nanocrystals [68] has since developed into a blossoming and fruitful field of research (for an overview see Ref. [69]. See also [70,71] for more recent work). Edgar and Gray [72] studied the effect of 2000 kDa dextran ( $R_g = 34$  nm) on the phase behaviour of cellulose nanocrystals (average length  $L = 110$  nm, average diameter  $D = 10$  nm), prepared by acid hydrolysis of cotton filter paper.

In Fig. 8.21, we redraw the I–N phase behaviour at low dextran concentrations. Above 7 wt % suspensions of these cellulose nanocrystals start to phase separate in an isotropic and chiral nematic liquid crystal phase. At 13.3 wt %, the relative volume of chiral nematic phase (compared to the total volume) is 79%. This wide biphasic range is a direct consequence of the polydispersity of the cellulose nanocrystals [35,73] and has been observed in other dispersions containing polydisperse rod-like colloids as well [15,74]. When dextran was added to the biphasic region, it led to a significant broadening of the coexistence region and the dextran preferentially partitions in the isotropic phase. These features are in agreement with the theory described in Sect. 8.4.

### 8.5.3 Sterically Stabilised Colloidal Boehmite Rods Mixed with Polymer

As mentioned in the introduction of this chapter, suspensions of rod-like inorganic colloids were the first systems in which the I–N transition was observed. In the early 1960s, Zocher and Torök [75–77] and Bugosh [78] observed interesting liquid

**Fig. 8.21** Influence of blue dextran ( $R_g/D = 3.4$ ) concentration (normalised to  $\phi_p$ ) on the isotropic–nematic phase coexistence in dispersions of rod-like cellulose nanorods ( $L/D = 11$ ) with volume fraction  $\phi$ . Replotted from Edgar and Gray [72]

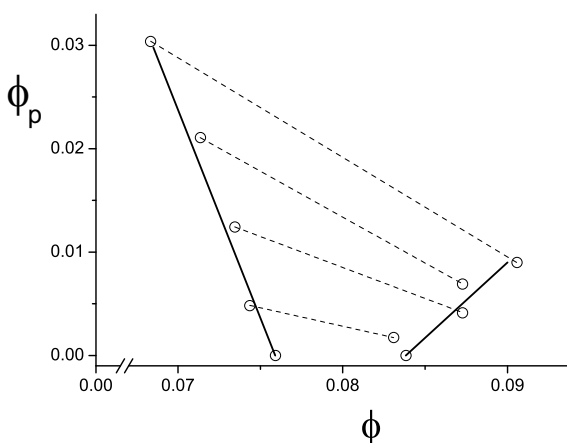


**Fig. 8.22** TEM micrograph of boehmite rods. Image kindly provided by J. Buitenhuis, Forschungszentrum Jülich, Germany

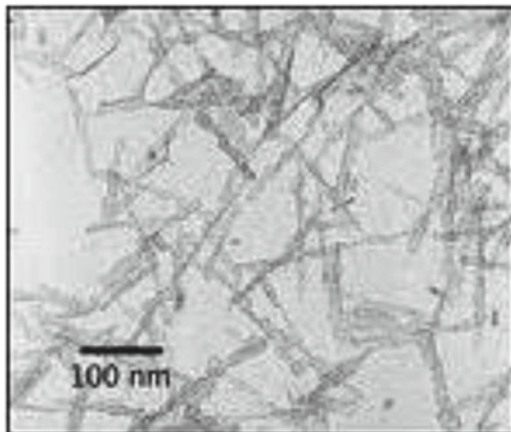
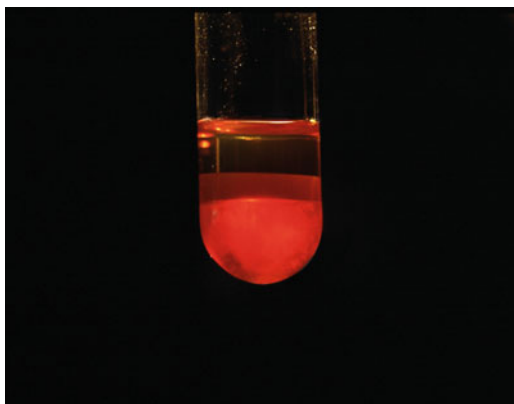


**Fig. 8.23** Triphasic  $I_1$ – $I_2$ – $N$  equilibrium in dispersions of boehmite rods and polystyrene chains in *ortho*-dichlorobenzene [79]. Image kindly provided by J. Buitenhuis, Forschungszentrum Jülich, Germany



crystal phase behaviour in aqueous dispersions of colloidal boehmite rods, shown in Fig. 8.22.

Later, Buining and Lekkerkerker [74] observed isotropic–nematic phase separation in a dispersion of sterically stabilised boehmite rods, which approximate hard rods, in cyclohexane. Buitenhuis et al. [79] studied the effect of added 35 kDa polystyrene ( $R_g = 5.9$  nm) on the liquid crystal phase behaviour of sterically stabilised boehmite rods with average  $L = 71$  nm and average  $D = 11.1$  nm in *ortho*-dichlorobenzene. Different phase equilibria were observed: two biphasic I–N equilibria (both dilute isotropic phase  $I_1$  with nematic N and concentrated isotropic phase  $I_2$  with nematic N) and a triphasic equilibrium  $I_1$ – $I_2$ –N (Fig. 8.23). In this system, the boehmite rods are quite polydisperse. Therefore, comparison with theory should be done with an approach that includes polydisperse rods (see, for instance, Refs. [33, 80]). We further note no  $I_1$ – $I_2$  coexistence was observed experimentally but rather an  $I_1$ –gel at high polymer concentrations. The depletant-mediated appearance of a nonequilibrium long-lived metastable state such as a gel resembles the behaviour of colloidal sphere/polymer mixtures (see Chap. 4).

## 8.6 Phase Diagrams of Rod/polymer Mixtures Including Highly Ordered Phases

In the previous sections we focused on the isotropic–nematic phase transition in mixed suspensions of rod-like colloids and flexible polymers. In Sect. 8.3, it was shown that scaled particle theory (SPT) provided the pressure and chemical potential of the hard spherocylinder reference system. SPT also enabled a route for the calculation of the free volume fraction, the quantities required in the FVT calculation of the phase diagram (see Sect. 8.4). Depending on  $L/D$  and  $\delta/D$ , three types of phase diagrams were obtained (presented in Fig. 8.10). For intermediate  $q$  values, a significant broadening of the I–N biphasic region was obtained. For large  $q$  values an isostructural  $I_1$ – $I_2$  transition arises in addition, while for small  $q$  values an additional  $N_1$ – $N_2$  transition arises. The broadening of the biphasic I–N region and also a triphasic  $I_1$ – $I_2$ –N equilibrium have indeed been observed experimentally in mixed suspensions of rod-like colloids and flexible polymers [60,72,79]. We noted that the theoretical prediction of the  $N_1$ – $N_2$  transition (which, so far, has not been observed experimentally in mixed suspensions of rod-like colloids and flexible polymers) should be treated with reservation.

The  $N_1$ – $N_2$  phase transition is predicted to occur at quite high volume fractions of rods. At these high volume fractions, the  $N_1$ – $N_2$  transition may be superseded by more highly ordered (liquid) crystal phases such as the colloidal smectic phase. Experimentally, this colloidal smectic phase has been observed [24,50,81] in suspensions of monodisperse rods. Simulations confirmed that hard rods can form a thermodynamically stable smectic phase [25–27,82]. In this section, we outline how the more dense highly ordered phases can be accounted for in the phase diagram of mixtures of rod-like colloids and flexible polymers using FVT.

### 8.6.1 Full Phase Diagrams of Hard Spherocylinders

Computer simulation results of suspensions containing hard spherocylinders [25–27] revealed that, with increasing concentration, isotropic (I), nematic (N), smectic–A (SmA), AAA crystal and ABC crystal phases appear as preferred phase states (Fig. 8.3a).

As discussed in Sect. 8.2.1, the rods have a random orientation in phase I, while, in the other phases, they are aligned along a common nematic director. Both I and N phases are fluids and have no long-range positional order. While SPT [43] provides a reasonable equation of state for long rods, Parsons–Lee (PL) theory [83–85] is more accurate for short rods. PL theory is basically an extension of the Carnahan–Starling equation of state and is discussed in more detail in Sect. 9.2.2. See also [31]. To accurately cover the full range of aspect ratios, Peters et al. [20] combined SPT and PL using a sigmoidal interpolation procedure. In the SmA, AAA and ABC phases, the particles are confined in layers and the nematic director is perpendicular to the layers. For the SmA phase, there is, however, still no positional order within the layers, while, in the AAA and ABC phases, the particles are ordered hexagonally. In

the AAA phase, the rods of adjacent layers are stacked on top of each other, while, in the ABC phase, they are stacked in between the rods of adjacent layers. For all three phase states, an extended cell theory was developed by Peters et al. [20], based upon an approach proposed by Graf and Löwen [86]. The final results were cast into algebraic equations [20], which are summarised below.

In general, for any of these phases, the free energy can be split into an ideal, orientational and packing contribution:

$$\tilde{F} = \frac{F v_0}{kTV} = \tilde{F}_{\text{id}} + \tilde{F}_{\text{or}} + \tilde{F}_{\text{pack}}, \quad (8.62)$$

with  $\tilde{F}_{\text{id}} = \phi \ln(\phi \Lambda^3 / v_c) - \phi$  being independent of the phase state and  $\tilde{F}_{\text{or}} = s[f]$  given by Eq. (8.3). For the SmA phase, the cell model includes a thermodynamic description of 2D discs with area fraction  $\phi_{2D}$  that captures the in-plane fluidity of rods projected onto the smectic plane. The expression for the packing free energy  $\tilde{F}_{\text{pack}}$  of the smectic phase reads

$$\begin{aligned} \frac{\tilde{F}_{\text{pack}}^{\text{SmA}}}{\phi} &= -\ln(1 - \phi_{2D} \bar{D}_{\text{eff}}^2) \\ &+ \frac{\phi_{2D} \bar{D}_{\text{eff}}^2}{1 - \phi_{2D} \bar{D}_{\text{eff}}^2} - \ln\left(1 - \frac{\Gamma}{\bar{\Delta}_{\perp}}\right). \end{aligned} \quad (8.63)$$

The quantities  $\bar{D}_{\text{eff}}$  and  $\bar{\Delta}_{\perp}$  in Eq. (8.63), as well as  $\tilde{F}_{\text{or}}$ , can be determined by simultaneously minimising the total free energy with respect to  $f(\Omega)$  and  $\bar{\Delta}_{\perp}$  (see Ref. [20] for details). The effective rod diameter  $\bar{D}_{\text{eff}}$  can be calculated using

$$D_{\text{eff}} = 1 + A(\Gamma - 1) \int f(\Omega) |\sin(\theta)| d\Omega, \quad (8.64)$$

where  $A$  was chosen such as to fit the resulting equations of state and nematic–smectic-A phase transitions to those obtained from computer simulations [26,27]. The quantity  $A$  varies depending on whether the equations of state for the nematic phase is based on SPT ( $A = 0.41\phi$ ) or PL ( $A = 0.28\phi$ ). For the sigmoidal interpretation approach  $A = 0.41\phi h$ , with  $h = g + (1 - g)0.28/0.41$ , with  $g$  defined by [20,21]

$$g = \frac{1}{1 + e^{\Gamma_t - \Gamma}}, \quad (8.65)$$

with  $\Gamma_t = 6$ , connecting the Onsager limit ( $\Gamma \rightarrow \infty$ ) and the sphere limit ( $\Gamma \rightarrow 1$ ).

For the AAA phase, Peters et al. [20] derived

$$\begin{aligned} \tilde{F}_{\text{pack}}^{\text{AAA}} &= \phi + \phi \ln \phi_{\text{cp}}^{\text{AAA}} - \phi \ln \left( \bar{\Delta}_{\parallel}^{\text{AAA}} - \bar{D}_{\text{eff}} \right)^2 \\ &- \phi \ln \left( \frac{\phi_{\text{cp}}^{\text{AAA}} / \phi}{(\bar{\Delta}_{\parallel}^{\text{AAA}})^2} - 1 \right), \end{aligned} \quad (8.66)$$

where for AAA the parameter  $A = 0.225\phi h$  in the definition of  $\bar{D}_{\text{eff}}$  was chosen based on comparison with simulation results for the equations of state and the AAA–ABC phase transition [26, 27]. The resulting normalised layer spacing  $\bar{\Delta}_{\parallel}$  reads

$$\bar{\Delta}_{\parallel}^{\text{AAA}} = \frac{6^{1/3} \left( \frac{\phi_{\text{cp}}^{\text{AAA}}}{\phi} \right) + \left( 9 \frac{\phi_{\text{cp}}^{\text{AAA}}}{\phi} + \frac{\phi_{\text{cp}}^{\text{AAA}}}{\phi} \sqrt{3 \left( 27 - 2 \frac{\phi_{\text{cp}}^{\text{AAA}}}{\phi} \right)} \right)^{2/3}}{6^{2/3} \left( 9 \frac{\phi_{\text{cp}}^{\text{AAA}}}{\phi} + \frac{\phi_{\text{cp}}^{\text{AAA}}}{\phi} \sqrt{3 \left( 27 - 2 \frac{\phi_{\text{cp}}^{\text{AAA}}}{\phi} \right)} \right)^{1/3}}. \quad (8.67)$$

The spacing parameter  $\Delta_{\parallel}$  is normalised through  $\bar{\Delta}_{\parallel} = \Delta_{\parallel}/D$ .

For the ABC crystal phase, an extended cell theory approach leads to the following expression [20, 86]:

$$\frac{\tilde{F}_{\text{pack}}^{\text{ABC}}}{\phi} = 1 + \ln \phi_{\text{ref}} - \ln \left( \bar{\Delta}_{\parallel}^{\text{ABC}} - \bar{D}_{\text{eff}} \right)^2 - \ln \left( \frac{\phi_{\text{ref}}/\phi}{(\bar{\Delta}_{\parallel}^{\text{ABC}})^2} - 1 \right), \quad (8.68)$$

with

$$\bar{\Delta}_{\parallel}^{\text{ABC}} = \frac{6^{1/3} \left( \frac{\phi_{\text{ref}}}{\phi} \right) + \left( 9 \frac{\phi_{\text{ref}}}{\phi} + \frac{\phi_{\text{ref}}}{\phi} \sqrt{3 \left( 27 - 2 \frac{\phi_{\text{ref}}}{\phi} \right)} \right)^{2/3}}{6^{2/3} \left( 9 \frac{\phi_{\text{ref}}}{\phi} + \frac{\phi_{\text{ref}}}{\phi} \sqrt{3 \left( 27 - 2 \frac{\phi_{\text{ref}}}{\phi} \right)} \right)^{1/3}},$$

and

$$\phi_{\text{ref}} = \frac{\pi (3\Gamma - 1)}{6 \left( \sqrt{3} (\Gamma - 1) + B\sqrt{2} \right)},$$

including the parameter  $B = 1.16$ . Next, the accuracy of these expressions is compared to computer simulation results.

For  $L/D = 4$ , the rod concentration dependence of the resulting theoretical osmotic pressures (curves) of the I, N, SmA and ABC phase states are plotted in Fig. 8.24. The predictions are compared to computer simulation data of McGrother et al. [26]. It is clear the equations of states correspond reasonably well to the computer simulation data. For comparisons at other aspect ratios, see Ref. [20].

Phase coexistence between two phases can be established by imposing mechanical and chemical equilibrium expressed by equality of osmotic pressure  $P$  and chemical potential  $\mu$  (Appendix A). Algebraic expressions for  $P$  and  $\mu$  were derived [20] for all phase states of the hard spherocylinders from the free energy expressions given above.

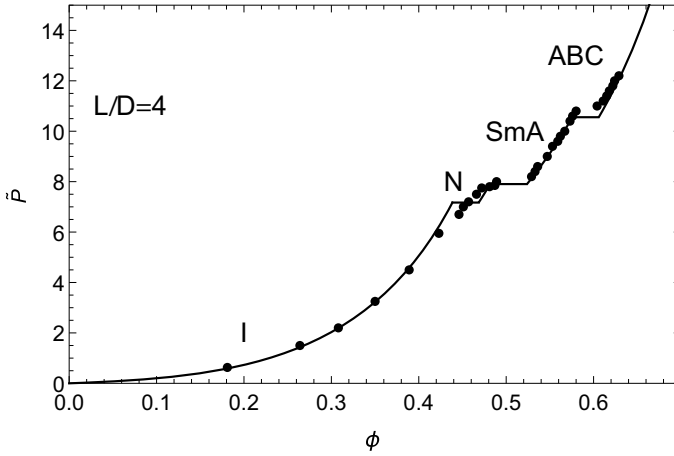


**Fig. 8.24** Osmotic pressure of hard spherocylinders with  $L/D = 4$  as a function of rod volume fraction  $\phi$  from both theory (solid curves) [20] and computer simulation results (data points) [26]. The stable phases include the isotropic (I), nematic (N), smectic-A (SmA), AAA crystal and ABC crystal phases

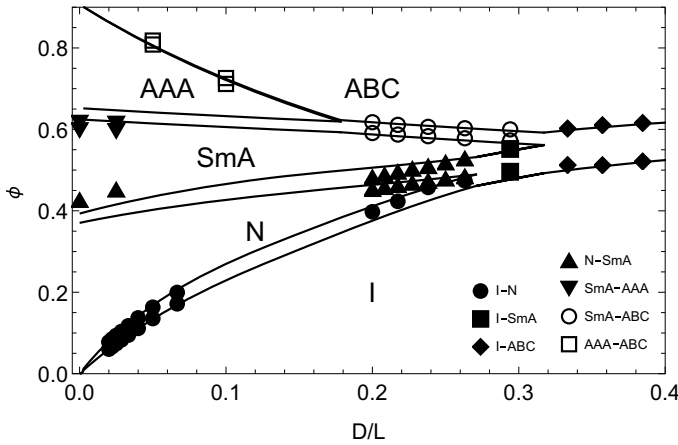


**Fig. 8.25** Phase behaviour of hard spherocylinders as a function of rod volume fraction  $\phi$  and aspect ratio  $D/L$  from both theory (solid curves) [20] and simulation (data points) [27]. The stable phases include the isotropic (I), nematic (N), smectic-A (SmA), AAA crystal and ABC crystal phases

The theoretical predictions [20] for the binodals using the analytical equations of states for all hard spherocylinder phase states discussed are shown in Fig. 8.25 (solid curves) as a function of volume fraction  $\phi$  and aspect ratio  $D/L$ . Computer simulation data of Bolhuis and Frenkel [27] are plotted as data points. The phase diagram of rods without endcaps (see Ref. [82]) is very close to these results.

It is noted (not shown) that in the sphere limit of  $L/D \rightarrow 0$  the equations of state for the isotropic and ABC phases become equivalent to those of a hard-sphere fluid and an FCC crystal, respectively (see Sect. 3.2.3). The agreement with the computer simulation results is quite reasonable for these phase equilibria.

### 8.6.2 Phase Behaviour of Rod–Polymer Mixtures Including Highly Ordered Phases

Next, the phase behaviour of mixtures of rod-like colloidal particles and polymers is considered, including the highly ordered phases discussed in the previous subsection. The rods are again described as hard spherocylinders and the nonadsorbing polymers are treated as ideal depletants by describing them as PHSs with radius  $\delta$  (see Chaps. 2 and 3). It is possible to explicitly include polymer–polymer interactions (see Chap. 4), which demonstrates that the PHS approximation for the polymer works well for the relatively small polymers discussed here. Hence, phase diagrams are discussed for mixtures of hard spherocylinders and PHSs.

The mixture is again described using FVT. The hard spherocylinder–PHS system of interest is in contact with a PHS reservoir through a semi-permeable membrane that is impermeable to the colloids but fully permeable for the polymers. Solvent plays the role of continuum background again.

We use Eq. (8.43) for  $\tilde{\Omega}$ , which we rewrite here as

$$\tilde{\Omega} = \tilde{F} - \alpha \tilde{\Pi}^R, \quad (8.69)$$

with  $\tilde{\Omega} = \Omega v_c / kTV$  as the normalised semi-grand potential for the system of interest, and  $\tilde{F} = F v_c / kTV$  as the normalised Helmholtz free energy for a pure dispersion of hard spherocylinders. The free volume fraction  $\alpha = \langle V_{\text{free}} \rangle / V$  is the average fraction of the system volume available to PHSs, and  $\tilde{\Pi}^R$  is the normalised osmotic pressure of the polymers in the reservoir, which is proportional to the reservoir polymer coil volume fraction  $\phi_p^R$  by  $\tilde{\Pi}^R = \phi_p^R (3\Gamma - 1) / (2q^3)$ .

A representative set of phase diagrams for colloid–polymer mixtures is shown in Fig. 8.26 in terms of the polymer reservoir concentration  $\phi_p^R$  versus the rod volume fraction  $\phi$  (see Refs. [21, 87, 88]). The rod aspect ratio is fixed at  $L/D = 12$  and polymer–rod size ratio is set to  $q = 0.4, 0.525$  and  $0.57$ . In the plots, the binodals (solid curves) and three- and four-phase coexistences (dashed lines) are shown. In most cases, the miscibility gaps widen as the polymer concentration is increased. At the points where two binodals coincide, there is three-phase coexistence. For instance, at  $q = 0.4$  (left panel) the miscibility gap of N–SmA and SmA–AAA coexistence widens as  $\phi_p^R$  increases. At around  $\phi = 0.4\text{--}0.65$  and  $\phi_p^R \approx 0.05$ , the binodals coincide and a triple N–SmA–AAA equilibrium emerges.

Increasing the polymer size qualitatively changes the phase diagram. The trends are similar to those reported by Savenko and Dijkstra [89] in their Monte Carlo simulation study. For example, at  $q = 0.57$  (right panel) the N–SmA binodal coincides

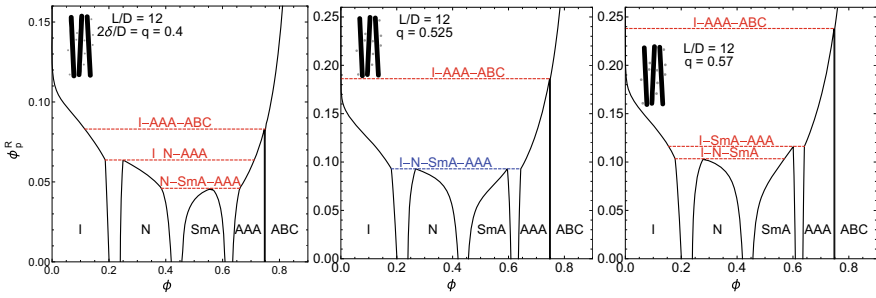


**Fig. 8.26** Phase diagrams of colloid–polymer mixtures in terms of the colloid volume fraction  $\phi$  and polymer reservoir concentration  $\phi_p^R$  for colloidal rods of aspect ratio  $L/D = 12$  and polymers of size  $q = 2\delta/D = 0.4$  (left),  $0.525$  (middle), and  $0.57$  (right). Binodals are displayed as solid curves, while three- and four-phase coexistences are indicated as dashed lines. Reprinted with permission from Ref. [87] under the terms of CC-BY-4.0

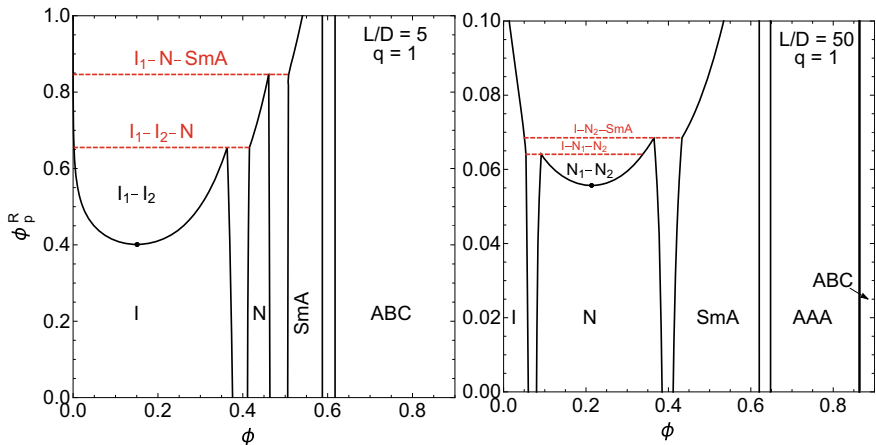


**Fig. 8.27** Phase diagrams of colloid–polymer mixtures in a similar representation as Fig. 8.26, but for parameters exhibiting isotropic  $I_1$ – $I_2$  (left) and  $N_1$ – $N_2$  (right) phase coexistence. The colloidal rods have an aspect ratio  $L/D = 5$  (left) and  $L/D = 50$  (right) and the polymers have a fixed size  $2\delta = D$ , so  $q = 1$ . Binodals are displayed as solid curves, while three-phase coexistences are indicated as dashed lines

with the I–N binodal and instead leads to a triple I–N–SmA coexistence. Similarly, the N–AAA and I–N–AAA coexistences are only present at the smaller  $q = 0.4$ , while the I–SmA binodals and I–SmA–AAA triphasic coexistence are only stable at  $q = 0.57$ . The intermediate polymer size of  $q = 0.525$  (middle panel) marks the exact size ratio where all three binodals coincide at the same polymer reservoir concentration. This leads to an I–N–SmA–AAA four-phase coexistence.

Next, the isostructural phase coexistences [88] discussed in Sect. 8.4 are re-evaluated. In Fig. 8.27, two examples are given for  $L/D = 5$  and  $L/D = 50$  and  $q = 1$ . As could be expected, the  $I_1$ – $I_2$  coexistence region (left panel) is large for sufficiently large polymer sizes compared to the rod length. For  $L/D = 50$  and  $q = 1$  (right panel), a region where  $N_1$ – $N_2$  phase equilibria are predicted appears.

This is not superseded by  $I_1$ – $SmA_2$  or  $I$ –crystalline phase equilibria. So, although these  $N_1$ – $N_2$  phase equilibria have not been observed they also appear as results from theoretical calculations when taking higher ordered phases of the rods into account. Moreover, the calculations reveal that (non-metastable) isostructural phase equilibria are possible for all phase states [21].

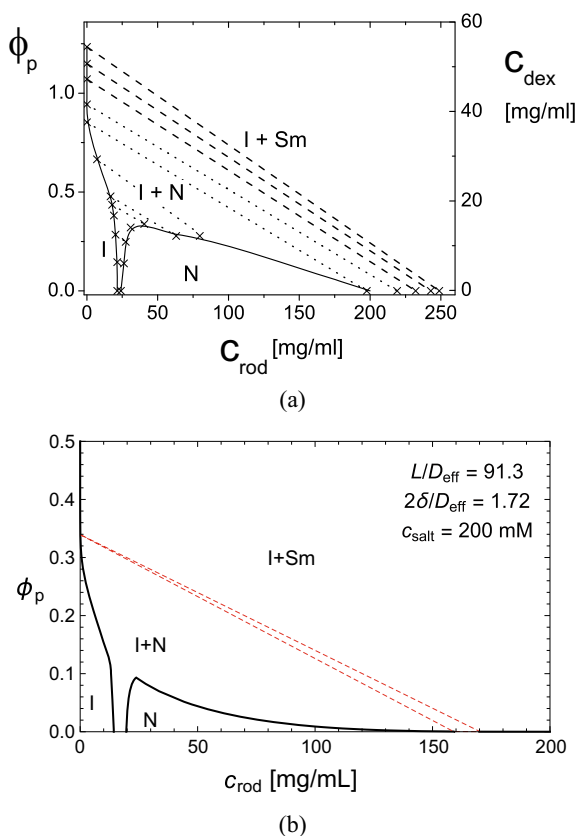


**Fig. 8.28** Phase diagrams of dextran/*fd*-virus mixtures. Data points are measured coexistences at an ionic strength of 200 mM and pH = 8.10. In addition to the isotropic–nematic coexistence (dotted coexistence lines), isotropic–smectic coexistence (dashed lines) is found at high polymer and rod concentrations. Replotted from Ref. [90]. **b** Predicted phase diagram of a hard spherocylinder–penetrable hard-sphere dispersion. Spherocylinders were modelled with  $L/D = 133$ ,  $D_{eff} = 9.64$  nm,  $L/D_{eff} = 91.31$ , an ionic strength of 200 mM and mixed with PHSs with  $2\delta/D_{eff} = 1.72$ . The dextran polymers have  $R_g = 11$  nm, the charge density is taken as  $-10$  e/nm to mimic the system of **a**. Solid curves represent  $I$ – $N$  phase equilibria. The dashed lines represent  $I$ – $N$ – $Sm$  triple coexistence. Above the triple region, there is  $I$ – $Sm$  phase coexistence

### 8.6.3 Comparison with Experiments

We now compare predictions including higher ordered phases with the limited number of experiments that have been reported in the literature. Dogic [90] extended the earlier work of Dogic and Fraden [60] on mixed suspensions of *fd* and dextran to higher dextran concentrations at a salt concentration of 200 mM. The phase diagram he observed is plotted in Fig. 8.28a. Above dextran concentrations of 55 mg/mL the I–N transition is superseded by the I–SmA transition. In Fig. 8.28b the predicted phase diagram is plotted for the relevant size parameters. The effective diameter of the rods was calculated using the theory presented in Sect. 8.2.2. The phase diagram computed corresponds to the experimental one. No observations were reported on the (narrow) triphasic I–N–SmA equilibrium that is expected between the biphasic I–N and I–SmA phase equilibria.

An interesting aspect of bacteria is that they can assume a wide range of shapes [91, 93], examples of which are shown in Fig. 8.29. In 1954 Goldacre [92] showed that, like viruses, some bacteria can be crystallised. The bacterial cells form regular three-dimensional arrays, in which each cell corresponds to a molecule in a conventional crystal. In the case of rod-shaped bacteria, the rods align in a parallel fashion, as shown in Fig. 8.30 for *Amoeba proteus* [92].

Experimental work [94–96] demonstrated that, upon exceeding a certain concentration, suspensions of (non-motile) bacteria and nonadsorbing polymers exhibit phase separation, just as colloid–polymer mixtures. Guided by the ideas of Goldacre [92], we apply free volume theory to describe this phase separation. We highlight the work presented by Schwarz-Linek et al. [95], who focused on mixtures of *Escherichia coli* (*E. coli*) (Fig. 8.31) and sodium polystyrene sulfonate (NaPSS).

The added NaPSS polymers have a molar mass of 64.7 kDa and a radius of gyration of 14 nm. The mixtures were studied in aqueous solutions containing 0.18 M salt, at which the Debye screening length is 0.8 nm. In Fig. 8.32, we present results of the phase behaviour of a suspension of *E. coli* bacteria with a volume fraction of 12.5% with different polymer weight fractions ranging from 0 to 10%.

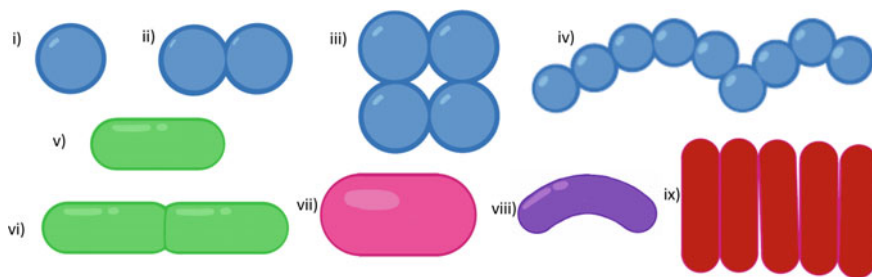


**Fig. 8.29** Examples of bacteria and their shapes. Cocci have a spherical to ovoid shape and appear not only as single cells (i) but also as pairs (e.g., Diplococci) (ii), clusters (e.g., tetrad) (iii) or chains (e.g., Streptococci) (iv). Bacilli (v) and Diplobacilli (vi) are rod-shaped bacteria. Coccobacilli (vii) resemble cocci and bacilli. Spiral bacteria (viii) are slightly curved microbes with a comma shape. Pallisades are bacteria with a picket fence structure of connected rods (ix). Sketches made by Luuk Tuinier, inspired by Ref. [91]

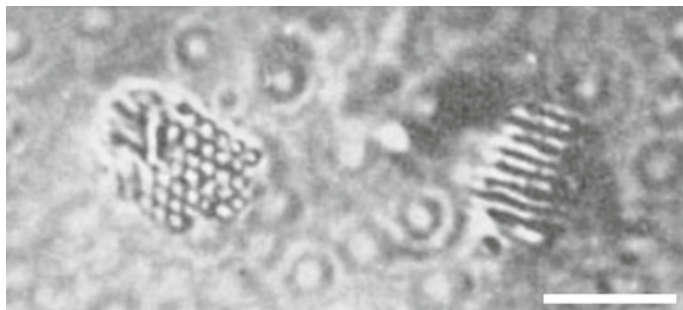
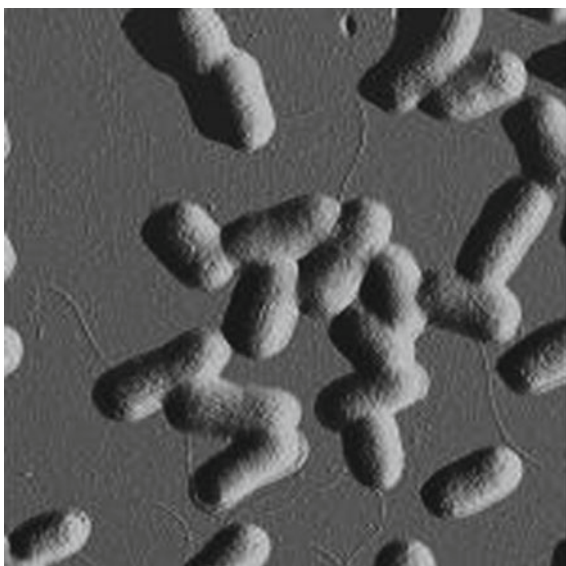


**Fig. 8.30** Microscopy image of three-dimensional arrays of *Amoeba proteus* bacteria. Scale bar represents 10  $\mu\text{m}$ . Reprinted with permission from Ref. [92]. Copyright 1954 Nature

**Fig. 8.31** AFM image of short, rod-like, *E. coli* bacteria. The width of the image represents 10  $\mu\text{m}$ . Reprinted with permission from Ref. [95]. Copyright 2010 RSC

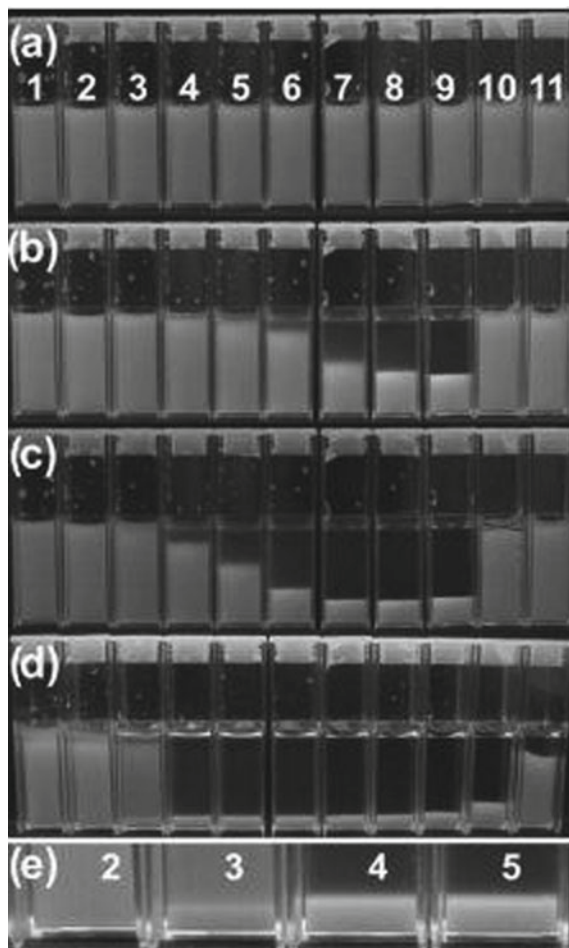


The pictures in Fig. 8.32 shows that the phase transition for a bacterial suspension of a volume fraction of 12.5% takes place at a polymer weight fraction of about 0.2% and that the bacterial volume fraction of the concentrated phase has a volume fraction of about 70%.

For the calculation of the phase behaviour, we assume that the *E. coli* bacteria (see Fig. 8.31) can be modelled as spherocylinders with  $L = D \approx 1 \mu\text{m}$ . We present calculations for the phase separation between the isotropic phase and the ABC crystal phase.

Schwarz-Linek et al. [95] present no experimental evidence that the concentrated phase is an ABC crystal, but it is known from the work of Goldacre [92] that such phases can occur in suspension of bacteria. By applying the theory presented in Sect. 8.6.2, we obtain the phase diagram plotted in Fig. 8.33b (see Ref. [97]).

**Fig. 8.32** *E. coli* cell samples (cell density  $\approx 9.6 \cdot 10^{10}$  cfu/mL ( $\phi \approx 0.125$ )) dispersed in phosphate buffer with NaPSS polyelectrolytes. The polymer concentration (in weight fraction) increases from left to right, with samples 1–11 containing 0%, 0.1%, 0.2%, 0.3%, 0.4%, 0.5%, 0.75%, 1%, 2%, 5% and 10% of NaPSS, respectively. Times: **a**  $t=0$ , **b**  $t=30$  min, **c**  $t=100$  min, **d**  $t=24$  h. **e** Shows the bottom parts of samples 2–5 at 24 h at higher magnification. Reprinted with permission from Ref. [95]. Copyright 2010 RSC



In Fig. 8.33b, the drawn curves are the result of the theoretical calculations. The datapoints are experimental results, indicating that the system shows (●) a single-phase or (+) two-phase coexistence. The free volume calculations are in good agreement with the experiments on phase separation in mixed suspensions of non-motile bacteria and nonadsorbing polymers. For more details, see Ref. [97].

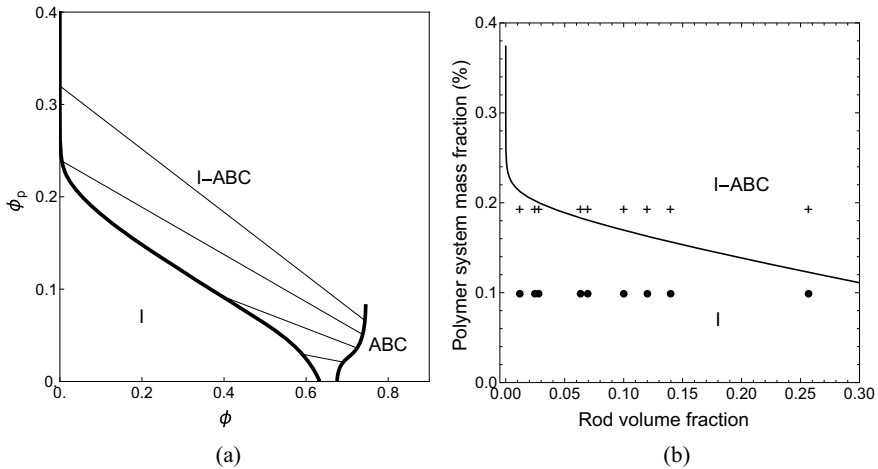


**Fig. 8.33** Phase diagram of hard spherocylinders ( $L/D = 1$ ) mixed with polymers ( $q = 2R_g/D = 0.028$ ). **a** Predicted isotropic–ABC crystal phase coexistence (thick curves) with a few illustrative tie-lines (thin lines) [97]. **b** Comparison between predictions (curve) and experimental observations of single-phase (●) or two-phase (+) systems [95]

## References

- Solomon, M.J., Spicer, P.T.: *Soft Matter* **6**, 1391 (2010)
- De Gennes, P.G., Prost, J.: *The Physics of Liquid Crystals*. Oxford University Press, Oxford (1974)
- Zocher, H., Anorg, Z.: *Chem.* **147**, 91 (1925)
- Bawden, F.C., Pirie, N.W., Bernal, J.D., Fankuchen, I.: *Nature* **138**, 1051 (1936)
- Livage, J.: *Chem. Mat.* **3**, 578 (1991)
- Vroege, G.J., Thies-Weesie, D.M.E., Petukhov, A.V., Lemaire, B.J., Davidson, P.: *Adv. Mat.* **18**, 2565 (2006)
- Buining, P.A., Philipse, A.P., Lekkerkerker, H.N.W.: *Langmuir* **10**, 2106 (1994)
- Maeda, H., Maeda, Y.: *Langmuir* **12**, 1446 (1996)
- Hosseini, S.N., Grau-Carbonell, A., Nikolaenkova, A.G., Xie, X., Chen, X., Imhof, A., van Blaaderen, A., Baesjou, P.J.: *Adv. Funct. Mater.* **30**, 2005491 (2020)
- V. Sharma, K. Park, M. Srinivasarao, *Mater. Sci. Eng.: R: Rep.* **65**, 1 (2009)
- Li, L.S., Walda, J., Manna, L., Alivisatos, A.P.: *Nano Lett.* **2**, 557 (2002)
- Kuijk, A., van Blaaderen, A., Imhof, A.: *J. Am. Chem. Soc.* **133**, 2346 (2011)
- Amara, M.S., Paineau, E., Bacia-Verloop, M., Krapf, M.E.M., Davidson, P., Belloni, L., Levard, C., Rose, J., Launois, P., Thill, A.: *Chem. Commun.* **49**, 11284 (2013)
- Wada, K., Yoshinaga, N., Yotsumoto, H., Ibe, K., Aida, S.: *Clay Miner.* **8**, 487 (1970)
- Zhang, Z.X., van Duijneveldt, J.S.: *J. Chem. Phys.* **124**, 154910 (2006)
- Fraden, S., Hurd, A.J., Meyer, R.B., Cahoon, M., Caspar, D.L.D.: *J. Phys. Colloques* **46**, C3 (1985)
- Dong, X.M., Kimura, T., Revol, J.F., Gray, D.G.: *Langmuir* **12**, 2076 (1996)
- P. Buining. personal communication
- Z. Dogic, S. Fraden, in *Soft Matter: Complex Colloidal Suspensions*, vol. 2, ed. by G. Gompper, M. Schick (John Wiley & Sons, Ltd, 2006), chap. 1, pp. 1–86
- Peters, V.F.D., Vis, M., Wensink, H.H., Tuinier, R.: *Phys. Rev. E* **101**, 062707 (2020)

21. V.F.D. Peters, Phase behaviour of mixtures of structurally complex colloids and polymers. Ph.D. thesis, Eindhoven University of Technology (2021)
22. Kuijk, A., Byelov, D.V., Petukhov, A.V., van Blaaderen, A., Imhof, A.: *Faraday Discuss.* **159**, 181 (2012)
23. Wetter, C.: *Biol. unserer Zeit* **15**, 81 (1985)
24. Oster, G.: *J. Gen. Physiol.* **33**, 445 (1950)
25. Frenkel, D., Lekkerkerker, H.N.W., Stroobants, A.: *Nature* **332**, 822 (1988)
26. McGrother, S.C., Williamson, D.C., Jackson, G.: *J. Chem. Phys.* **104**, 6755 (1996)
27. Bolhuis, P.G., Frenkel, D.: *J. Chem. Phys.* **106**, 666 (1997)
28. Cohen, S.S.: *J. Biol. Chem.* **144**, 353 (1942)
29. Leberman, R.: *Virology* **30**, 341 (1966)
30. Onsager, L.: *Ann. NY Acad. Sci.* **51**, 627 (1949)
31. Vroege, G.J., Lekkerkerker, H.N.W.: *Rep. Progr. Phys.* **55**, 1241 (1992)
32. Herzfeld, J., Berger, A.E., Wingate, J.W.: *Macromolecules* **17**, 1718 (1984)
33. Lekkerkerker, H.N.W., Coulon, P., van der Haegen, R., Deblieck, R.: *J. Chem. Phys.* **80**, 3427 (1984)
34. van Roij, R.: *Eur. J. Phys.* **26**, S57 (2005)
35. Odijk, T., Lekkerkerker, H.N.W.: *J. Phys. Chem.* **89**, 2090 (1985)
36. Odijk, T.: *Macromolecules* **19**, 2313 (1986)
37. Franco-Melgar, M., Haslam, A.J., Jackson, G.: *Mol. Phys.* **106**, 649 (2008)
38. Verwey, E.J.W., Overbeek, J.T.: *Theory of the Stability of Lyophobic Colloids*. Elsevier, Amsterdam (1948)
39. Stroobants, A., Lekkerkerker, H.N.W., Odijk, T.: *Macromolecules* **19**, 2232 (1986)
40. Philip, J., Wooding, R.: *J. Chem. Phys.* **52**, 953 (1970)
41. Hill, T.L.: *Arch. Biochem. Biophys.* **57**, 229 (1955)
42. van der Schoot, P., Odijk, T.: *J. Chem. Phys.* **97**, 515 (1992)
43. Cotter, M.A.: *J. Chem. Phys.* **66**, 1098 (1977)
44. Lekkerkerker, H.N.W., Stroobants, A.: *Il Nuovo Cimento D* **16**, 949 (1994)
45. Tuinier, R., Taniguchi, T., Wensink, H.H.: *Eur. Phys. J. E* **23**, 355 (2007)
46. Fraden, S., Maret, G., Casper, D.L.D., Meyer, R.B.: *Phys. Rev. Lett.* **63**, 2068 (1989)
47. Yamakawa, H.: *Modern Theory of Polymer Solutions*. Harper and Row, New York (1971)
48. Strobl, G.: *The Physics of Polymers*, 3rd edn. Springer, Berlin Heidelberg New York (2007)
49. Adams, M., Fraden, S.: *Biophys. J.* **74**, 669 (1998)
50. Dogic, Z., Fraden, S.: *Phys. Rev. Lett.* **78**, 2417 (1997)
51. Grelet, E.: *Phys. Rev. X* **4**, 021053 (2014)
52. Zimmermann, K., Hagedorn, H., Heuck, C., Hinrichsen, M., Ludwig, H.: *J. Biol. Chem.* **261**, 1653 (1986)
53. Janmey, P.A., Slochower, D.R., Wang, Y.H., Wen, Q., Cēbers, A.: *Soft Matter* **10**, 1439 (2014)
54. Secor, P.R., Sweere, J.M., Michaels, L.A., Malkovskiy, A.V., Lazzareschi, D., Katznelson, E., Rajadas, J., Birnbaum, M.E., Arrigoni, A., Braun, K.R., Evanko, S.P., Stevens, D.A., Kaminsky, W., Singh, P.K., Parks, W.C., Bollyky, P.L.: *Cell Host Microbe* **18**, 549–559 (2015)
55. Tarafder, A.K., von Kūgelgen, A., Mellul, A.J., Schulze, U., Aarts, D.G.A.L., Bharat, T.A.M.: *Proc. Natl. Acad. Sci.* **117**, 4724 (2020)
56. Urakami, N., Imai, M., Sano, Y., Tasaku, M.: *J. Chem. Phys.* **111**, 2322 (1999)
57. Sano, Y.: *Macromol. Symp.* **99**, 239 (1995)
58. Imai, M., Urakami, N., Nakamura, A., Takada, R., Oikawa, R., Sano, Y.: *Langmuir* **18**, 9918 (2002)
59. Levy, J.A., Fraenkel-Conrat, H., Owens, R.A.: in: *Virology*. Prentice Hall, Englewood Cliffs, New Jersey (1994)
60. Dogic, Z., Fraden, S.: *Phil. Trans. R. Soc. Lond. A* **359**, 997 (2001)
61. Dogic, Z., Purdy, K.R., Grelet, E., Adams, M., Fraden, S.: *Phys. Rev. E* **69**, 051702 (2004)
62. Holmqvist, P., Ratajczyk, M., Meier, G., Wensink, H.H., Lettinga, M.P.: *Phys. Rev. E* **80**, 031402 (2009)
63. Barry, E., Beller, D., Dogic, Z.: *Soft Matter* **5**, 2563 (2009)

64. Huisman, E.M., Wen, Q., Wang, Y.H., Cruz, K., Kitenbergs, G., Erglis, K., Zeltins, A., Cebers, A., Janmey, P.A.: *Soft Matter* **7**, 7257 (2011)
65. Booy, F.P., Fowler, A.G.: *Int. J. Biol. Macromol.* **7**, 327 (1985)
66. Wettstadt, S.: *Environ. Microbiol.* **22**, 2461 (2020)
67. Marchessault, R.H., Morehead, F.F., Walters, N.M.: *Nature* **184**, 632 (1959)
68. Habibi, Y., Lucia, L.A., Rojas, O.J.: *Chem. Rev.* **110**(6), 3479 (2010)
69. M. Roman, W.T. Winter, *TAPPI Techn. Papers* **06NANO09**, 5 (2006)
70. Oguzlu, H., Danumah, C., Boluk, Y.: *Curr. Opin. Colloid Interface Sci.* **29**, 46–56 (2017)
71. Oguzlu, H., Boluk, Y.: *Cellulose* **24**, 131–146 (2017)
72. Edgar, C.D., Gray, D.G.: *Macromolecules* **35**, 7400 (2002)
73. Vroege, G.J., Lekkerkerker, H.N.W.: *J. Phys. Chem.* **97**, 3601 (1993)
74. Buining, P.A., Lekkerkerker, H.N.W.: *J. Phys. Chem.* **97**, 11510 (1993)
75. Zocher, H., Torök, C.: *Kolloid Z.* **170**, 140 (1960)
76. Zocher, H., Torök, C.: *Kolloid Z.* **173**, 1 (1960)
77. Zocher, H., Torök, C.: *Kolloid Z.* **180**, 41 (1962)
78. Bugosh, J.: *J. Phys. Chem.* **65**, 1791 (1961)
79. Buitenhuis, J., Donselaar, L.N., Buining, P.A., Stroobants, A., Lekkerkerker, H.N.W.: *J. Colloid Interface Sci.* **175**, 46 (1995)
80. Wensink, H.H., Vroege, G.J.: *J. Chem. Phys.* **119**, 6868 (2003)
81. Kreibitz, U., Wetter, C.: *Z. Naturforsch.* **35C**, 750 (1980)
82. Lopes, J.T., Romano, F., Grelet, E., Franco, L.F.M., Giacometti, A.: *J. Chem. Phys.* **154**, 104902 (2021)
83. Parsons, J.D.: *Phys. Rev. A* **19**, 1225 (1979)
84. Lee, S.D.: *J. Chem. Phys.* **87**, 4972 (1987)
85. Lee, S.D.: *J. Chem. Phys.* **89**, 7036 (1988)
86. Graf, H., Löwen, H.: *Phys. Rev. E* **59**, 1932 (1999)
87. V.F.D. Peters, M. Vis, Á. González García, H.H. Wensink, R. Tuinier, *Phys. Rev. Lett.* **125**, 127803 (2020)
88. V.F.D. Peters, Á. González García, H.H. Wensink, M. Vis, R. Tuinier, *Langmuir* **37**, 11582 (2021)
89. S.V. Savenko, M. Dijkstra, *J. Chem. Phys.* **124** (2006)
90. Dogic, Z.: *Phys. Rev. Lett.* **91**, 165701 (2003)
91. Yang, D.C., Blair, K.M., Salama, N.R.: *Microbiol. Mol. Biol. Rev.* **80**, 187 (2016)
92. Goldacre, R.J.: *Nature* **174**, 732 (1954)
93. Typas, A., Banzhaf, M., Gross, C., Vollmer, W.: *Nat. Rev. Microbiol.* **10**, 123–136 (2012)
94. Schwarz-Linek, J., Dorken, G., Winkler, A., Wilson, L.G., Pham, N.T., French, C.E., Schilling, T., Poon, W.C.K.: *Europhys. Lett.* **89**, 68003 (2010)
95. Schwarz-Linek, J., Winkler, A., Wilson, L.G., Pham, N.T., Schilling, T., Poon, W.C.K.: *Soft Matter* **6**, 4540 (2010)
96. Dorken, G., Ferguson, G.P., French, C.E., Poon, W.C.K., Soc, J.R.: *Interface* **9**, 3490 (2012)
97. Peters, V.F.D., Vis, M., Tuinier, R., Lekkerkerker, H.N.W.: *J. Chem. Phys.* **154**, 151101 (2021)

**Open Access** This chapter is licensed under the terms of the Creative Commons Attribution 4.0 International License (<http://creativecommons.org/licenses/by/4.0/>), which permits use, sharing, adaptation, distribution and reproduction in any medium or format, as long as you give appropriate credit to the original author(s) and the source, provide a link to the Creative Commons license and indicate if changes were made.

The images or other third party material in this chapter are included in the chapter's Creative Commons license, unless indicated otherwise in a credit line to the material. If material is not included in the chapter's Creative Commons license and your intended use is not permitted by statutory regulation or exceeds the permitted use, you will need to obtain permission directly from the copyright holder.

